# U–Pb geochronology and geochemistry of Bibi-Maryam pluton, eastern Iran: Implication for the late stage of the tectonic…

**Article** *in* Lithos · July 2014

DOI: 10.1016/j.lithos.2014.04.015



**5 authors**, including:

Morteza Delavari
Kharazmi University


Sadraddin Amini
University of California, Los Angeles


Kevin Mckeegan
University of California, Los Angeles

Lithos 200–201 (2014) 197–211

Contents lists available at ScienceDirect

Lithos

journal homepage: www.elsevier.com/locate/lithos

# U–Pb geochronology and geochemistry of Bibi-Maryam pluton, eastern Iran: Implication for the late stage of the tectonic evolution of the Sistan Ocean

Morteza Delavari [a,*], Sadraddin Amini [b], Axel K. Schmitt [b], Kevin D. McKeegan [b], T. Mark Harrison [b]

[a] Department of Geochemistry, Faculty of Earth Science, Kharazmi University, 49 Mofatteh Avenue, P.O. Box 15614, Tehran, Iran
[b] Department of Earth and Space Sciences, University of California Los Angeles, 595 Charles Dr. E, Los Angeles, CA 90095-1567, USA

ARTICLE INFO

*Article history:*
Received 10 September 2013
Accepted 16 April 2014
Available online 2 May 2014

*Keywords:*
Adakite
Slab-melting
Sistan suture zone
Iran

ABSTRACT

The Bibi-Maryam pluton crops out in the Sistan suture zone, eastern Iran. This pluton is a 1.5 × 2 km stock composed of leucocratic tonalite, granodiorite and granite. U–Pb zircon geochronology of a leucogranite indicates an emplacement age of 58.6 ± 2.1 Ma (95% confidence). The Bibi-Maryam rock suite is sodic with elevated $Na_2O/K_2O$ (2.9 to 5.5), Sr/Y (15.6–62.2), La/Yb (13.3–22.2), and low MgO (0.86–1.81) abundances. It lacks significant Eu anomalies. Because of these geochemical characteristics, Bibi-Maryam rocks are similar to high-$SiO_2$ adakites. Trace element modeling indicates that the Bibi-Maryam adakitic rocks could be produced by 5–8% non-modal batch partial melting from a source with composition of 95% N-MORB + 5% sediment in the presence of 35–40% amphibole + 5–10% garnet + 55–60% clinopyroxene + 1% apatite + 1% rutile. This source mineralogy is similar to hornblende eclogite or garnet amphibolites. Collectively, these data provide new constraints for the evolution of the Sistan suture zone and suggest that the Bibi-Maryam pluton formed via slab melting in an oceanic arc and pre-plate collision tectonic setting. This implies that the closure of the Sistan Ocean and Lut–Afghan continental blocks collision happened after the Bibi-Maryam emplacement at 58.6 ± 2.1 Ma.



## 1. Introduction

Ophiolitic remnants within the Alpine–Himalayan orogenic belt result from the juxtaposition of continental blocks after closure of Tethyan oceans. During the Cimmerian orogeny and accompanying closure of Paleo-Tethys and opening of Neo-Tethys, various continental fragments accreted to Eurasia including the Sanandaj–Sirjan, Alborz and Central-East Iranian Microcontinents (CEIM) with the Lut block in the eastern part of the CEIM assembly (e.g., Stampfli, 2000; Wilmsen et al., 2009; Zanchi et al., 2009). In southern Iran, Neo-Tethyan suturing during the Late Cretaceous (Alavi, 1994; Berberian and King, 1981; Mohajjel and Fergusson, 2000), Eocene (Ghasemi and Talbot, 2006; Mazhari et al., 2009) or Miocene (e.g., Bird et al., 1975; Mohajjel et al., 2003; Sengör and Kidd, 1979) led to the collision of the Arabian and central Iran platforms along the Main Zagros Thrust (Stöcklin, 1977). The ophiolitic fragments now exposed along the Zagros fold-and-thrust belt including Kermanshah and Sawlava ophiolites (e.g. Allahyari et al., 2010, 2014; Saccani et al., 2013) represent the remnants of Neo-Tethyan Ocean locating between the Arabian shield and Cimmerian terranes. According to Allahyari et al. (2010) and Saccani et al. (2013) crustal and mantle suites in the Kermanshah ophiolites preserve evidence for various stages of oceanic basin evolution from an early phase of rifting to a developed ocean which thereafter experienced oceanic plate consumption via an intra-oceanic subduction. Likewise, in the Sawlava ophiolitic complex (Kurdistan area), mineral and whole rock chemistry of ultramafic cumulates are consistent with a boninitic magmatism defining a forearc magmatic scenario associated with an intra-oceanic arc system (Allahyari et al., 2014). It is also worth noting that another exposure of ophiolitic complex inside the Zagros orogen and to the south of the Main Zagros Thrust, the Neyriz ophiolite, shows island arc magmatic signatures and was linked to a supra-subduction zone environment (Babaie et al., 2006).

In the central to eastern domain of Iran, the ophiolitic outcrops around CEIM namely "Inner Zagros ophiolite belt" of Stöcklin (1968) including Shahr-e-Babak, Nain, Baft, Sabzevar, Tchehel Kureh, Nehbandan and Birjand ophiolites (e.g., Arvin and Robinson, 1994; Desmons and Beccaluva, 1983; Khalatbari Jafari et al., 2013; Saccani et al., 2010; Shafaii Moghadam and Stern, 2011) delineate a fossil oceanic seaway encompassing CEIM (e.g., McCall, 1997). The presumably extensional regime and development of new oceanic basins surrounding the CEIM during the Jurassic–Cretaceous is subject of debate, and has been variably attributed to slab rollback of the Neo-Tethyan ocean and complete detachment of CEIM from Eurasia, or to a back-arc basin development (Bagheri and Stampfli, 2008 and references therein; Rossetti et al., 2010). Although, based on supra-subduction zone affinity in mantle

* Corresponding author. Tel.: +98 21 88309293.
*E-mail addresses:* delavarimza@gmail.com, delavari@khu.ac.ir (M. Delavari).

http://dx.doi.org/10.1016/j.lithos.2014.04.015
0024-4937/

tectonites and overlying magmatic rocks and also age similarities, some of these components such as Nain–Baft ophiolitic exposures along with Neyriz and Kermanshah ophiolites and coeval ophiolitic remnants in Turkey, Cyprus and Oman have been assumed as disrupted segments of once-continuous oceanic fore-arc formed during the Late Cretaceous time along the southern margin of Eurasia (Shafaii Moghadam and Stern, 2011; Shafaii Moghadam et al., 2013).

The Sistan suture zone in eastern Iran contains ophiolitic rocks representing remnants of an oceanic basin that was part of a Neo-Tethyan branch between the CEIM and Afghan continental block (Fig. 1a) (e.g. Saccani et al., 2010; Tirrul et al., 1983). Previous geological studies of the Sistan suture zone as one of the key areas recording the Neo-Tethyan collision (e.g., Camp and Griffis, 1982; Tirrul et al., 1983: Delavari, 2010; Pang et al., 2012, 2013; Saccani et al., 2010; Zarrinkoub et al., 2012) documented an abundance of magmatic rocks in the Sistan suture zone (Camp and Griffis, 1982; Pang et al., 2013; Sadeghian et al., 2005) whose ages and petrogenetic classification undergirded tectonomagmatic models for the area (Pang et al., 2012, 2013). However, critical details regarding emplacement ages, tectonic setting and petrological and geochemical characteristics of the Sistan suture zone magmatic rocks remain poorly understood. One of the most contentious points is the timing of the closure of the Sistan Ocean which has been assigned to the Late Cretaceous (Zarrinkoub et al., 2010) or Eocene (Camp and Griffis, 1982; Tirrul et al., 1983). Recent tectonomagmatic model of Zarrinkoub et al. (2012) assumes a Late Cretaceous time for the collision of the Lut–Afghan continental blocks based on radiometric ages for magmatic rocks with adakitic affinity in the range of 86–71 Ma (Zarrinkoub et al., 2010). In this study, we use U–Pb zircon geochronology and major and trace element geochemistry of Bibi-Maryam plutonic rocks that indicate intra-oceanic arc formation and slab melting at ~59 Ma to propose a much younger collisional age for the Lut–Afghan continental blocks.

## 2. Geological setting

The Sistan suture zone is a north–south trending tectonic contact zone in eastern Iran approximately from Birjand in the north to Zahedan in the south. It separates two microcontinental blocks, the Lut block (to the west) and Afghan block (to the east) (Fig. 1a, b). This zone was initially an oceanic basin whose age and closure mechanisms remain debated. Based on Tirrul et al. (1983), the Sistan Ocean formed in the Late Cretaceous and finally closed in the Middle to Late Eocene. In accordance with Tirrul et al. (1983), rock units older than Upper Cretaceous have not been mapped for the Sistan suture zone (Alavi Naini et al., 1990; Guillou et al., 1983; Tirrul et al., 1989). Within the Nehbandan ophiolitic complex located north-east of Nehbandan town (Fig. 1b), pelagic limestones of Turonian age exist (Delavari, 2010). Other regional ophiolitic units (e.g., south of Nosrat Abad and west of Zahedan in

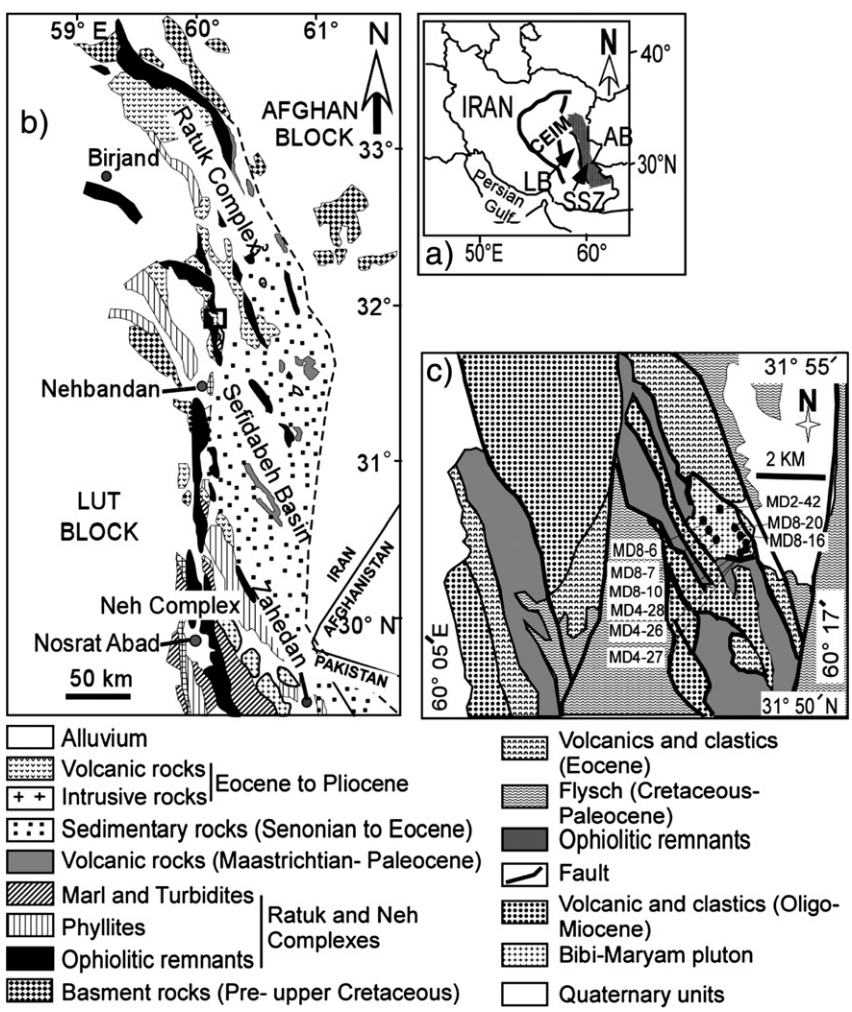


**Fig. 1.** a) Generalized tectonic map of Iran showing the locations of Central-East Iranian Microcontinent (CEIM), Lut block (LB), Sistan suture zone (SSZ) and Afghan block (AB). b) Geological sketch map of the Sistan suture zone (modified after Tirrul et al., 1983). The box indicates the location of the study area. c) Simplified geological map of the study area and location of the studied samples.

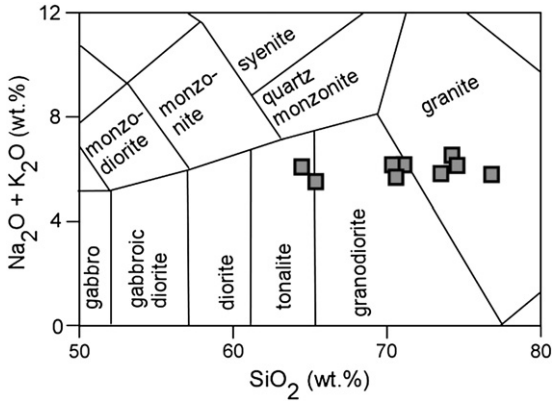


**Fig. 2.** Total alkali-silica classification diagram for Bibi-Maryam pluton (Middlemost, 1994).

Fig. 1b) yielded K/Ar age between 60 and 100 Ma (Delaloye and Desmons, 1980). This is at variance with Lower Cretaceous (Aptian and Albian) radiolarites reported for the Gazik province of the Sistan suture zone, which imply that the Sistan Ocean predates the Upper Cretaceous (Babazadeh and De Wever, 2004). Moreover, U–Pb zircon dating of Birjand ophiolite rocks has revealed Lower Cretaceous ages between 113 ± 1 and 107 ± 1 Ma for its formation age (Zarrinkoub et al., 2012). These findings suggest that the Sistan Ocean could date to the Lower Cretaceous. Fotoohi Rad et al. (2009) used $^{40}Ar/^{39}Ar$ geochronology of eclogite, blueschist and amphibolites from the Gazik and Sulabest area with ages of c. 116–139 Ma to propose that peak metamorphism and subsequent retrograde epidote–amphibolite-facies overprint occurred prior to c. 125 Ma. These results conflict with Rb–Sr, $^{40}Ar/^{39}Ar$ and U–Pb ages in Bröcker et al. (2013) who dated similar rocks from the field area of Fotoohi Rad et al. (2009), but obtained younger ages of 85–87 Ma.

**Table 1**
Whole rock major and trace element analyses of Bibi-Maryam granitoids. Mg# = 100 × Mg/(Mg + $Fe^{2+}$). b.d.l. = below detection limit.

| Sample | MD2-42 | MD4-26 | MD4-27 | MD4-28 | MD8-6 | MD8-7 | MD8-10 | MD8-16 | MD8-20 | MD8-10 |
|---|---|---|---|---|---|---|---|---|---|---|
| Rock type | Granite | Granodiorite | Granodiorite | Granodiorite | Granite | Granite | Tonalite | Tonalite | Granite | (Dup) |
| *ICP-ES analyses (wt.%)* | | | | | | | | | | |
| $SiO_2$ | 74.19 | 70.42 | 70.51 | 70.52 | 76.25 | 78.53 | 66.85 | 65.73 | 75.22 | |
| $TiO_2$ | 0.13 | 0.20 | 0.19 | 0.19 | 0.13 | 0.13 | 0.20 | 0.21 | 0.13 | |
| $Al_2O_3$ | 13.49 | 15.15 | 15.13 | 15.43 | 13.53 | 12.73 | 18.95 | 18.48 | 14.73 | |
| $Fe_2O_3$ | 0.18 | 0.26 | 0.24 | 0.25 | 0.16 | 0.08 | 0.17 | 0.26 | 0.13 | |
| FeO | 1.19 | 1.70 | 1.62 | 1.65 | 1.08 | 0.55 | 1.16 | 1.75 | 0.86 | |
| MnO | 0.05 | 0.05 | 0.05 | 0.05 | 0.07 | 0.05 | 0.09 | 0.08 | 0.06 | |
| MgO | 1.23 | 1.81 | 1.62 | 1.59 | 1.01 | 0.92 | 1.49 | 1.48 | 0.86 | |
| CaO | 2.00 | 3.44 | 3.29 | 3.43 | 0.92 | 1.05 | 4.83 | 4.54 | 1.77 | |
| $Na_2O$ | 5.43 | 4.72 | 4.87 | 4.86 | 5.14 | 4.97 | 4.47 | 4.74 | 4.43 | |
| $K_2O$ | 1.08 | 1.03 | 1.16 | 1.24 | 1.19 | 0.90 | 1.27 | 1.56 | 1.53 | |
| $P_2O_5$ | 0.09 | 0.09 | 0.08 | 0.09 | 0.10 | 0.09 | 0.11 | 0.09 | 0.10 | |
| LOI | 1.01 | 1.18 | 1.29 | 0.70 | 0.92 | 0.72 | 1.02 | 1.43 | 0.82 | |
| Total | 100.07 | 100.05 | 100.06 | 100.00 | 100.50 | 100.73 | 100.63 | 100.36 | 100.65 | |
| Mg# | 62.1 | 62.6 | 61.2 | 60.2 | 59.6 | 72.3 | 66.9 | 57.1 | 61.1 | |
| A/CNK | 0.98 | 1.00 | 0.99 | 0.99 | 1.19 | 1.15 | 1.08 | 1.04 | 1.21 | |
| *ICP-ES analyses (ppm)* | | | | | | | | | | |
| Sc | 2 | 3 | 1 | 2 | 2 | 2 | 3 | 3 | 2 | 3 |
| Cr | b.d.l. | b.d.l. | b.d.l. | b.d.l. | b.d.l. | b.d.l. | b.d.l. | b.d.l. | b.d.l. | b.d.l. |
| *ICP-MS analyses (ppm)* | | | | | | | | | | |
| Zn | 20 | 31 | 30 | 29 | 27 | 26 | 31 | 32 | 33 | |
| Cu | 4.8 | 7.1 | 7.1 | 6.2 | 26.1 | 28.3 | 19.9 | 19.5 | 12.8 | |
| Ga | 9.7 | 11.5 | 11.7 | 12.3 | 11.9 | 9.7 | 14.3 | 13.1 | 11.7 | 13.1 |
| Ni | 2.4 | 4.0 | 3.7 | 3.5 | 3.5 | 1.9 | 3.1 | 3.8 | 2.7 | |
| Co | 0.3 | 3.5 | 2.8 | 3.5 | 3.2 | 2.4 | 3.5 | 3.7 | 2.8 | |
| V | <8 | 13 | 11 | 10 | 11 | <8 | 15 | 19 | <8 | 15 |
| Ba | 164 | 166 | 175 | 177 | 249 | 201 | 174 | 197 | 231 | 176 |
| Rb | 30.3 | 29.8 | 32.8 | 34.5 | 35.8 | 27.4 | 38.9 | 48.4 | 43.7 | 38.2 |
| Sr | 204.5 | 262.0 | 272.7 | 261.9 | 154.5 | 141.7 | 373.3 | 341.1 | 194.4 | 354.8 |
| Y | 6.3 | 6.1 | 5.5 | 5.2 | 9.5 | 9.1 | 6.0 | 5.7 | 7.9 | 5.1 |
| Zr | 72.6 | 94.6 | 92.4 | 88.5 | 69.6 | 56.4 | 79.6 | 112.5 | 71.3 | 81.9 |
| Nb | 3.8 | 3.6 | 3.3 | 3.4 | 7.1 | 7.2 | 3.7 | 3.8 | 4.6 | 3.6 |
| La | 10.8 | 13.8 | 12.2 | 12.9 | 12.8 | 12.9 | 8.7 | 8.9 | 12.3 | 9.0 |
| Ce | 19.5 | 24.6 | 21.5 | 22.9 | 22.7 | 24.0 | 15.4 | 14.8 | 21.6 | 15.2 |
| Pr | 2.10 | 2.60 | 2.26 | 2.45 | 2.54 | 2.71 | 1.64 | 1.64 | 2.30 | 1.71 |
| Nd | 7.1 | 8.9 | 7.8 | 8.4 | 8.6 | 9.6 | 5.7 | 6.0 | 7.1 | 7.8 |
| Sm | 1.29 | 1.47 | 1.30 | 1.40 | 1.64 | 1.70 | 1.16 | 1.13 | 1.58 | 1.09 |
| Eu | 0.45 | 0.51 | 0.50 | 0.50 | 0.39 | 0.36 | 0.43 | 0.46 | 0.40 | 0.49 |
| Gd | 1.12 | 1.20 | 1.02 | 1.11 | 1.54 | 1.47 | 1.04 | 1.03 | 1.39 | 0.94 |
| Tb | 0.18 | 0.18 | 0.15 | 0.17 | 0.26 | 0.26 | 0.16 | 0.17 | 0.22 | 0.15 |
| Dy | 1.04 | 1.04 | 0.92 | 0.94 | 1.56 | 1.35 | 0.93 | 0.79 | 1.24 | 0.95 |
| Ho | 0.21 | 0.21 | 0.19 | 0.18 | 0.32 | 0.28 | 0.21 | 0.20 | 0.26 | 0.19 |
| Er | 0.60 | 0.61 | 0.57 | 0.53 | 0.87 | 0.75 | 0.63 | 0.58 | 0.77 | 0.48 |
| Tm | 0.09 | 0.10 | 0.09 | 0.09 | 0.14 | 0.14 | 0.09 | 0.10 | 0.11 | 0.08 |
| Yb | 0.65 | 0.67 | 0.63 | 0.58 | 0.96 | 0.83 | 0.63 | 0.69 | 0.91 | 0.60 |
| Lu | 0.11 | 0.13 | 0.11 | 0.11 | 0.15 | 0.15 | 0.12 | 0.12 | 0.13 | 0.09 |
| Hf | 1.9 | 2.3 | 2.3 | 2.2 | 2.0 | 1.9 | 1.9 | 2.8 | 2.1 | 2.1 |
| Ta | 0.3 | 0.3 | 0.3 | 0.3 | 0.5 | 0.4 | 0.2 | 0.3 | 0.4 | 0.2 |
| Th | 3.6 | 4.5 | 3.8 | 4.2 | 4.4 | 4.9 | 2.4 | 2.2 | 3.9 | 2.3 |
| U | 0.7 | 0.5 | 0.5 | 0.4 | 0.7 | 0.6 | 0.4 | 0.5 | 0.7 | 0.4 |

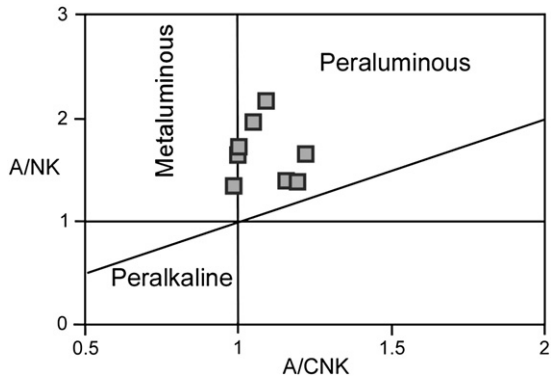


**Fig. 3.** A/NK vs. A/CNK diagram showing slightly metaluminous to peraluminous nature of the samples. A/NK = $Al_2O_3/(Na_2O + K_2O)$, A/CNK = $Al_2O3/(CaO + Na_2O + K_2O)$ (molar ratio).

The possibility that the Sistan Ocean predates the Cretaceous as noted by some authors (see Dercourt et al., 1986) would imply that the Afghan and Lut blocks were separated, and moved independently during the Jurassic–Earliest Cretaceous. This would also rule out that the Sistan Ocean was a basin created during Cretaceous rifting between the Lut–Afghan continental blocks (Tirrul et al., 1983). Equally controversial are models for the Sistan Ocean closure with various directions for the oceanic lithosphere subduction: east-northeast beneath Afghan continental block (Angiboust et al., 2013; Camp and Griffis, 1982; Saccani et al., 2010; Tirrul et al., 1983), westward beneath the Lut block (Pang et al., 2013; Zarrinkoub et al., 2012), or two-sided beneath both, the Lut and Afghan continental blocks (Arjmandzadeh et al., 2011).

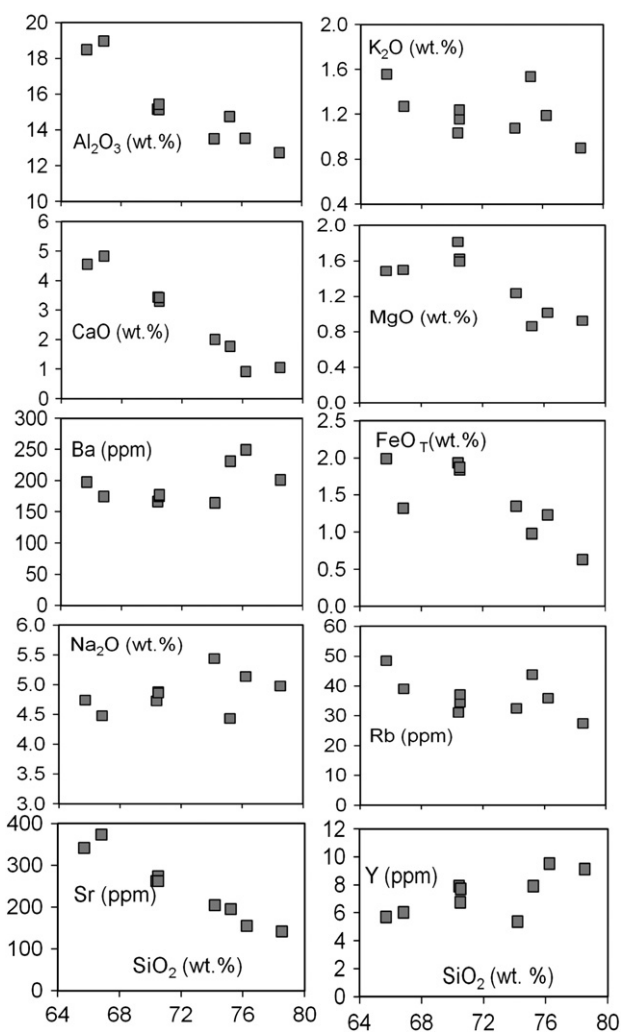


**Fig. 4.** Harker diagrams showing variation of selected major and trace elements vs. $SiO_2$ content.

The Sistan suture zone hosts ophiolitic remnants, marine sedimentary rocks, high- and low-grade metamorphics, and extensive magmatic rocks mostly in the form of volcanics and to a lesser extent plutonic rocks. On the basis of Tirrul et al. (1983), the Sistan suture zone can be divided into two geological terranes (Fig. 1b), the Neh–Ratuk complex and the Sefidabeh basin as an accretionary prism and forearc basin, respectively. The accretionary prism consists of a mélange of ophiolitic assemblages, Cretaceous to Eocene phyllite and Paleogene terrigenous marine sedimentary rocks and is subdivided into two smaller zones, the younger Neh complex to the southwest and the older Ratuk complex to the east. The forearc basin sediments onlap the accretionary complexes and consist of Cenomanian to Eocene marine sedimentary rocks. Along the Sistan suture zone, fragments of oceanic lithosphere have been preserved as obducted ophiolitic massifs which constitute about 30% of both, the Neh and Ratuk complexes.

Abundant Paleogene and Neogene calk-alkaline and alkaline magmatic rocks crop out in the Sistan suture zone (Camp and Griffis, 1982; Pang et al., 2012, 2013; Sadeghian et al., 2005). Cretaceous–Paleocene calk-alkaline volcanics in the eastern margin of Sefidabeh basin are the oldest magmatic rocks (Camp and Griffis, 1982). Extensive outcrops of plutonic rocks exist in the southern part of the Sistan suture zone. Among these, calk-alkaline I-type Zahedan granitoids dated to 31–33 Ma (Camp and Griffis, 1982) are the most extensive (Sadeghian et al., 2005).

The Bibi-Maryam pluton is located in the central part of the Sistan suture zone. Located 40 km to the northeast of Nehbandan town, it forms a prominent topographic high (2200 m elevation) and it extends over an area of 1.5 to 2 km. The Bibi-Maryam pluton is structurally enclosed within the different suture zone lithologies (Fig. 1c). Field

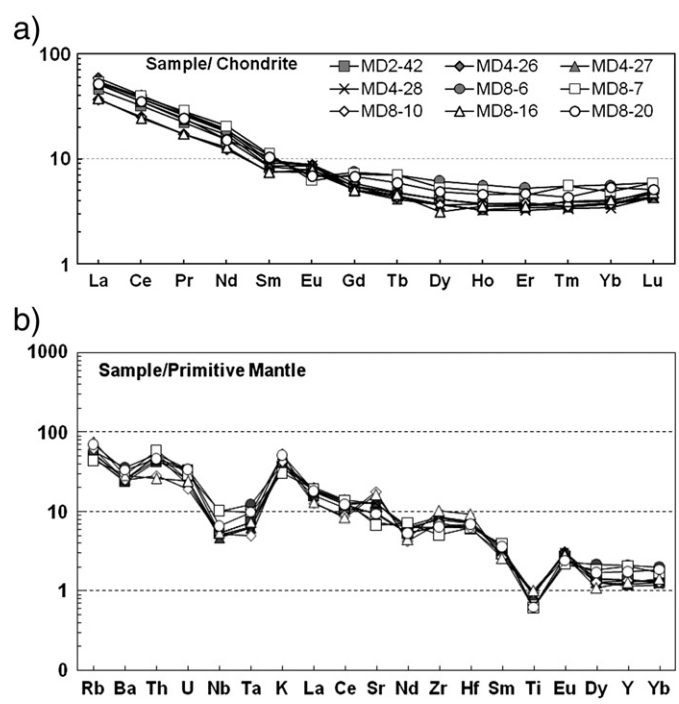


**Fig. 5.** a) Chondrite-normalized REE diagram. b) Primitive mantle-normalized multi-element diagram for Bibi-Maryam pluton. Chondrite and primitive mantle normalization values are from Sun and McDonough (1989).

relations indicate mostly fault contacts between the Bibi-Maryam pluton and neighboring country rocks including ophiolitic peridotite and Tertiary volcano-sedimentary associations. Primary contacts, however, are often obscured by later deformation or structural dislocations that can be attributed to its location along the trajectory of a minor branch of the active east-Neh fault. This major north–south right-lateral strike-slip fault is still active (Walker et al., 2009) and as a result, some outer parts of the pluton show mylonitic deformation fabrics.

## 3. Analytical techniques

Whole-rock major and trace element data were obtained by Inductively Coupled Plasma-Emission Spectrometry (ICP-ES) using a Spectro Ciros Vision instrument and Inductively Coupled Plasma-Mass Spectrometry (ICP-MS) on Perkin Elmer Elan 6000 instruments at AcmeLabs. The major elements and also Cr and Sc were determined by ICP-ES and the remaining trace elements by ICP-MS. It should be noted that among trace elements, Cu, Zn and Ni were obtained by Aqua Regia — ICP-MS analysis which include sample splits of 0.5 g leaching in hot (95 °C) Aqua Regia. Powdered rock samples were mixed with $LiBO_2/Li_2B_4O_7$ flux and fused in crucibles in a furnace. The quenched bead was dissolved in ACS grade nitric acid. Loss-on-ignition (LOI) was determined by heating a sample split to 1000 °C. Detection limits are as follows: $SiO_2$, $Al_2O_3$, CaO, MgO, $Na_2O$, MnO, $TiO_2$, $P_2O_5$ = 0.01%; $Fe_2O_3$, $K_2O$ = 0.04%; Cr = 15 ppm; LOI = 0.1%; Sc, Zn, Ba = 1 ppm; V = 8 ppm; Sr, Ga = 0.5 ppm; Nd = 0.3 ppm; Co, Th = 0.2 ppm; Cu, Hf, Nb, Ni, Rb, Ta, U, Y, Zr, La, Ce = 0.1 ppm; Yb, Dy, Gd, Sm = 0.05 ppm; Er = 0.03 ppm; Ho, Eu, Pr = 0.02 ppm; Lu, Tm, Tb = 0.01 ppm.

Major element composition of minerals was obtained by electron probe microanalyzer (EPMA), using a Jeol 8200 Superprobe at University of California, Los Angeles (UCLA). Operating condition was an acceleration voltage of 15 keV and five spectrometers with a focused beam and counting time of 15–20 s. Mineralogically matching standards were used for EPMA calibration.

U–Pb zircon geochronology was carried out at UCLA using a CAMECA *ims*1270 ion microprobe following procedures described by Schmitt et al. (2003a, b) and Quidelleur et al. (1997). Separation of zircon grains used standard heavy liquid and magnetic methods. Microdrilling of polished thin sections was also used for zircon separation. Both zircon grains and microdisks were epoxy-mounted with zircon standard AS3 from Duluth gabbro and polished. After carbon coating, the disks were imaged under the SEM (Scanning Electron Microscope, LEO 1430 VP, Oxford, EDAX, at UCLA, ESS) using a cathodoluminescence (CL) detector. For SIMS analysis, the carbon coating was removed, and replaced with a conductive gold layer. SIMS operating conditions were set to a mass resolution power m/Δ = 4500 at 10% of the peak height, and a secondary ion energy bandpass of 50 eV. The ion-beam was focused to a spot with a diameter of 15 to 20 μm. U/Pb relative sensitivity was calibrated by analyzing AS3 ($^{206}Pb/^{238}U$ age = 1099.1; Paces and Miller, 1993) interspersed with the unknowns.

## 4. Petrography and mineral chemistry

Petrographically, Bibi-Maryam plutonic rocks are mostly medium-grained, equigranular and mainly composed of plagioclase and quartz. Biotite is the main ferromagnesian mineral which is modally <1 to 3%. The Mg/(Fe + Mg) ratio ranges from 0.50 to 0.61 showing that biotite is enriched in Mg (Appendix A). Plagioclase is the volumetrically dominant phase (65–70% of the mode) and is generally subhedral to anhedral with varying grain size ranging from <1 to 4 mm in diameter. $Na_2O$, CaO and $K_2O$ contents in plagioclase are in the ranges of 5.59–9.78 wt.%, 3.37–10.46 wt.% and 0.05–0.26 wt.%, respectively. Plagioclase is mostly sodic with a compositional range of oligoclase to andesine (An = 16–50) (Appendix B). Orthoclase component in plagioclase is <1% which is consistent with highly sodic nature of the host rock. Plagioclase occasionally displays albite twinning and rarely zoning. K-feldspar as a separate phase is absent. Quartz modally ranges from 25 to 30% and generally appears as late-crystallized anhedral phase filling the interstitial spaces. Accessory minerals include sphene, zircon, apatite and Fe–Ti oxides, which totally are <1%. Although muscovite is present in some samples, it is secondary because it shows overgrowth on plagioclase and biotite and it occurs in zones that cut primary plagioclase and biotite. Other alteration minerals are present in some samples including sericite, chlorite, and epidote. Alteration is variable both in intensity and types of secondary mineralization. Plagioclase is altered to sericite, muscovite and chlorite. Biotite replacement by muscovite and chlorite ranges from absent to complete. Due to low-temperature mylonitization, ductile deformation is evident in some samples. This phenomenon is represented by rock foliation in macroscopic scale and recrystallization, subgrain and undulose extinction of quartz, preferred orientation and folding of sub-parallel biotite,

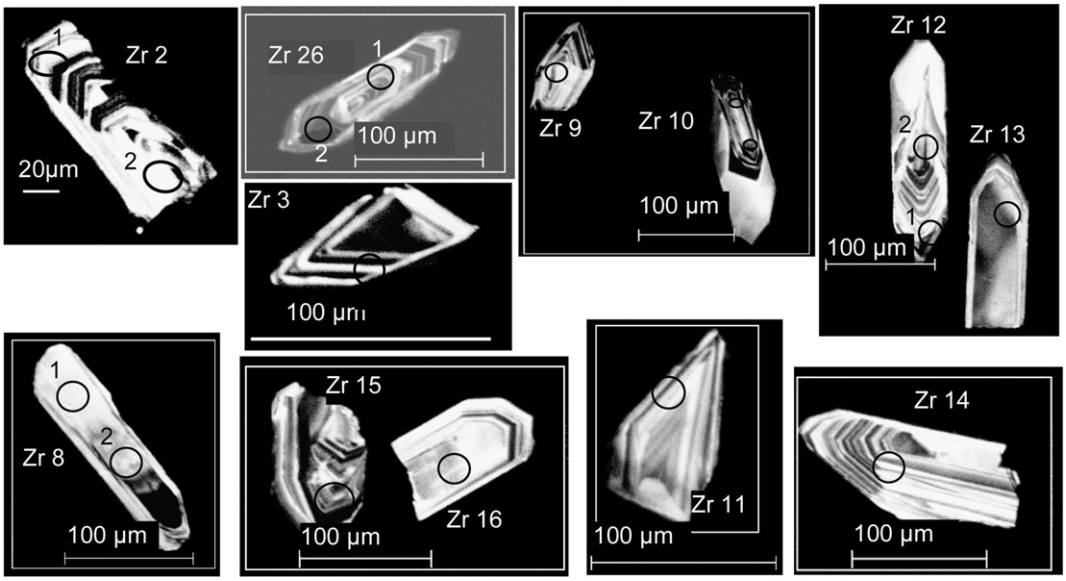


**Fig. 6.** Cathodoluminescence images of zircons from the Bibi-Maryam pluton. Circles mark the sites of analyses.

**Table 2**
Zircon U–Pb isotopic data and calculated ages for Bibi-Maryam pluton.

| | Age (Ma) | | | | | | $^{204}Pb/^{206}Pb$ | $^{204}Pb/^{206}Pb$ | % radiogenic | |
|---|---|---|---|---|---|---|---|---|---|---|
| | $^{207}Pb/^{235}U$ | $^{207}Pb/^{235}U$ | $^{206}Pb/^{238}U$ | $^{206}Pb/^{238}U$ | $^{207}Pb/^{206}Pb$ | $^{207}Pb/^{206}Pb$ | | | $^{206}Pb$ | $^{207}Pb^*/^{235}U$ |
| | | 1 σ | | 1 σ | | 1 σ | | 1 σ | | |
| Zr 2-1 | 59 | 8 | 57 | 2 | 117 | 325 | 0.0004 | 0.0004 | 99.7 | 0.0595 |
| Zr 2-2 | 63 | 6 | 59 | 3 | 207 | 210 | 0.0002 | 0.0002 | 99.8 | 0.0642 |
| Zr 10-1 | 65 | 5 | 63 | 3 | 136 | 155 | 0.0003 | 0.0003 | 99.6 | 0.0665 |
| Zr 10-2 | 64 | 8 | 63 | 3 | 118 | 262 | 0.0004 | 0.0004 | 99.6 | 0.0652 |
| Zr 11-1 | 63 | 9 | 55 | 2 | 342 | 301 | 0.0006 | 0.0005 | 99.9 | 0.0635 |
| Zr 12-1 | 104 | 17 | 97 | 7 | 258 | 343 | 0.0034 | 0.0008 | 96.2 | 0.107 |
| Zr 12-2 | 68 | 6 | 67 | 3 | 76 | 194 | b.d. | b.d. | 99.8 | 0.0690 |
| Zr 13-1 | 67 | 5 | 60 | 3 | 341 | 119 | 0.0003 | 0.0002 | 100.5 | 0.0685 |
| Zr 14-1 | 70 | 8 | 57 | 3 | 538 | 213 | 0.0003 | 0.0003 | 100.9 | 0.0719 |
| Zr 15-1 | 62 | 4 | 55 | 2 | 339 | 95 | 0.0001 | 0.0001 | 100.7 | 0.0634 |
| Zr 16-1 | 61 | 7 | 57 | 2 | 224 | 217 | b.d. | b.d. | 99.9 | 0.0620 |
| Zr 26-1 | 69 | 8 | 74 | 6 | – | – | 0.0008 | 0.0005 | 99.0 | 0.0704 |
| Zr 26-2 | 99 | 13 | 85 | 9 | 459 | 221 | 0.0004 | 0.0004 | 101.0 | 0.103 |
| Zr 8-1 | 66 | 11 | 60 | 4 | 305 | 319 | 0.0008 | 0.0007 | 99.4 | 0.0677 |
| Zr 8-2 | 69 | 11 | 58 | 4 | 465 | 321 | 0.0024 | 0.0017 | 99.8 | 0.0700 |
| Zr 9-1 | 48 | 5 | 56 | 3 | – | – | b.d. | b.d. | 98.9 | 0.0489 |
| Zr 3-1 | 91 | 17 | 86 | 5 | 214 | 411 | 0.0075 | 0.0007 | 87.1 | 0.0932 |

– = undefined.

muscovite and chlorite and mechanical twins of plagioclase in thin section.

## 5. Results

### 5.1. Major and trace element geochemistry

Based on chemical criteria using total alkali-silica diagram, the Bibi-Maryam pluton consists of tonalite, granodiorite and granite (Fig. 2). Whole-rock major element contents are characterized by $Al_2O_3$ contents ranging from 12.73 to 18.95 wt.% (Table 1). All samples show elevated $Na_2O/K_2O$ varying from 2.9 to 5.5 due to higher $Na_2O$ (4.43–5.43 wt.%) and lower $K_2O$ (0.9–1.56 wt.%) contents. Moreover, $TiO_2$ and $P_2O_5$ show low contents in the ranges of 0.13 to 0.21 wt.% and 0.08 to 0.11 wt.%, respectively. A/NK (molar ratio of $Al_2O_3/[Na_2O + K_2O]$) and A/CNK (molar ratio of $Al_2O_3/[CaO + Na_2O + K_2O]$) ranges from 1.34 to 2.17 and 0.98 to 1.21, respectively (Fig. 3) indicative of peraluminous to slightly metaluminous compositions. Whole-rock Mg# range from 57.1 to 72.3. Harker diagrams (Fig. 4) show negative correlations between $SiO_2$ and CaO, $Al_2O_3$ and Sr which suggest plagioclase fractionation or accumulation. MgO and FeO decrease with increasing $SiO_2$ (Fig. 4) implying fractionation of ferromagnesian minerals such as biotite and magnetite. Furthermore, Y demonstrates a weak positive correlation with $SiO_2$ suggesting an insignificant role of magmatic crystal fractionation of minerals with high mineral-melt partitioning coefficients for Y such as allanite, amphibole and apatite. $K_2O$, Rb and Ba lack systematic variations with $SiO_2$ abundance. As a whole, the major element variation diagrams suggest comagmatic relationships, via fractional crystallization between the more acidic evolved rocks and intermediate precursors.

Chondrite-normalized rare earth element (REE) abundances (Fig. 5a) show fractionated REE patterns with light REE (LREE) enrichment. $(La/Yb)_N$ ranges from 9.3 to 16 and $(Sm/Yb)_N$ from 1.8 to 2.7. All REE patterns show Eu anomalies with Eu/Eu* varying from 0.68 to 1.3, representing both minor negative and positive anomalies which are consistent with plagioclase fractionation and accumulation.

A primitive mantle-normalized multi element diagram (Fig. 5b) displays a subduction zone magmatic signature for Bibi-Maryam rocks. A negative anomaly of some HFSEs is revealed by pronounced troughs for Nb, Ta and Ti in the patterns. On the other hand, LILEs such as Rb and Ba show positive anomaly. Likewise, the spike in Th reveals the enrichment of this element relative to HFSEs such as Nb and Ta. Sr indicates a slight positive or negative anomaly which could be interpreted analogous to the Eu variations indicating plagioclase accumulation and fractionation.

### 5.2. U–Pb zircon geochronology

SIMS U–Pb dating was performed on 12 zircon grains separated from sample MD4-26 to obtain the formation age of the Bibi-Maryam pluton. This sample is modally 67% plagioclase, 30% quartz and 3% biotite. The zircon grains are mostly euhedral and prismatic in shape (the ratio of length to width is 2 to 5) and are less than 50 μm to nearly 150 μm in length (rarely >200 μm). CL images (Fig. 6) mostly show oscillatory or growth zoning, consistent with igneous origin and their growth by magmatic processes (Hoskin and Schaltegger, 2003).

13 out of 17 analyses show a homogeneous age distribution with a weighted average $^{206}Pb/^{238}U$ age of 58.6 ± 2.1 Ma (uncertainty at 95% confidence scaled by the square-root of the mean square of weighted deviates MSWD = 1.6) (Table 2; Fig. 7). The remaining four analyses are between ~74 and 97 Ma. Two spots on grain 26 yielded a reproducibly older age indicative of a potential crustal contaminant. There is only one spot on grain 3 which shows oscillatory zonation. Grain 12 yielded one older analysis in the finely-oscillatory domain of the crystal, whereas a younger domain with homogeneous CL replaces the finely-oscillatory zircon. This is consistent with resorption of an older zircon in an initially zircon-undersaturated melt. Because spots were typically placed in the oscillatory-zoned (and therefore likely magmatic) zircon domains, the age of 58.6 ± 2.1 Ma could represent a minimum for the emplacement age of the Bibi-Maryam pluton.

## 6. Interpretation

### 6.1. Adakitic nature of Bibi-Maryam pluton

Major and trace element contents of Bibi-Maryam pluton share many of the criteria put forward for adakite classification (Castillo, 2012; Defant and Drummond, 1990). This includes their high $Al_2O_3$ (12.7–19.0 wt.%), $Na_2O$ (4.43–5.43 wt.%) and Sr (142–373 ppm) contents, low MgO (0.86–1.81), Y (5–10 ppm) and Yb (0.6–1 ppm) values, and high Sr/Y (15.6–62.2) and La/Yb (13.3–22.2). Moreover, Eu anomalies are largely insubstantial, and indicative of minor plagioclase fractionation and accumulation. On the Sr/Y vs. Y diagram (Drummond and Defant, 1990), the samples fall within the adakite field (Fig. 8).

| $^{207}Pb^*/^{235}U$ 1 σ | $^{206}Pb^*/^{238}U$ | $^{206}Pb^*/^{238}U$ 1 σ | $^{207}Pb^*/^{206}Pb^*$ | $^{207}Pb^*/^{206}Pb^*$ 1 σ | Correlation of concordia ellipses | UO/U | UO/U 1 σ | U ppm | Th/U atomic |
|---|---|---|---|---|---|---|---|---|---|
| 0.0088 | 0.00892 | 0.000355 | 0.0484 | 0.0067 | 0.39 | 7.83 | 0.04 | 147 | 0.74 |
| 0.0067 | 0.00926 | 0.000419 | 0.0503 | 0.0045 | 0.51 | 7.69 | 0.04 | 302 | 0.64 |
| 0.0052 | 0.00990 | 0.000439 | 0.0488 | 0.0032 | 0.55 | 7.64 | 0.03 | 208 | 0.37 |
| 0.0087 | 0.00977 | 0.000528 | 0.0484 | 0.0054 | 0.59 | 7.62 | 0.06 | 187 | 0.26 |
| 0.0094 | 0.00864 | 0.000362 | 0.0533 | 0.0071 | 0.48 | 7.82 | 0.04 | 178 | 0.41 |
| 0.019 | 0.0152 | 0.00115 | 0.0514 | 0.0077 | 0.52 | 7.11 | 0.04 | 397 | 0.44 |
| 0.0066 | 0.0105 | 0.000493 | 0.0475 | 0.0039 | 0.53 | 7.48 | 0.02 | 348 | 0.88 |
| 0.0048 | 0.00933 | 0.000411 | 0.0533 | 0.0028 | 0.66 | 7.71 | 0.04 | 520 | 0.60 |
| 0.0082 | 0.00895 | 0.000460 | 0.0582 | 0.0057 | 0.54 | 7.66 | 0.05 | 229 | 0.76 |
| 0.0041 | 0.00864 | 0.000341 | 0.0532 | 0.0022 | 0.78 | 7.63 | 0.03 | 694 | 0.39 |
| 0.0068 | 0.00888 | 0.000384 | 0.0506 | 0.0048 | 0.54 | 7.70 | 0.05 | 246 | 0.86 |
| 0.0085 | 0.0116 | 0.000889 | 0.0442 | 0.0038 | 0.70 | 7.02 | 0.02 | 398 | 0.52 |
| 0.015 | 0.0133 | 0.00135 | 0.0562 | 0.0056 | 0.71 | 6.89 | 0.03 | 380 | 0.85 |
| 0.0112 | 0.00936 | 0.000657 | 0.0524 | 0.0073 | 0.54 | 7.49 | 0.07 | 116 | 0.66 |
| 0.0120 | 0.00902 | 0.000598 | 0.0563 | 0.0082 | 0.57 | 7.69 | 0.08 | 59 | 0.53 |
| 0.0056 | 0.00872 | 0.000429 | 0.0407 | 0.0041 | 0.46 | 7.73 | 0.05 | 157 | 0.42 |
| 0.0185 | 0.0134 | 0.000771 | 0.0504 | 0.0090 | 0.49 | 7.83 | 0.04 | 737 | 0.09 |

Based on $SiO_2$, MgO, and Sr contents, Sr/Y, K/Rb (270–300), $K_2O$ (0.90–1.56 wt.%) and Nb (3–7 ppm), the samples fall within the field of high-$SiO_2$ adakites (Fig. 9). It should be noted that in comparison with low-$SiO_2$ adakites, the high-$SiO_2$ adakites have lower Sr/Y and MgO, Sr and Nb abundances (Martin et al., 2005) which is in accordance with the comparatively low Sr abundances in our samples.

High Sr/Y and La/Yb coupled with low Y (<10 ppm) and HREE ($Yb_N$ < 5.6) abundances necessitate the absence of plagioclase as a residual phase in the source. Instead, these chemical characters implicate stable garnet, amphibole and clinopyroxene in the melting region (Castillo, 2012; Kay, 1978; Kay et al., 1991; Martin et al., 2005; Peacock et al., 1994). This requires an initial melt equilibration at high pressures, corresponding to a depth below the stability field of plagioclase (>30 km) along with the presence of garnet and amphibole (Castillo, 2012 and references therein). Scenarios that match these requirements for adakite generation include partial melting of thickened arc or thickened post-collisional continental crust (e.g. Chung et al., 2003; Petford and Atherton, 1996; Topuz et al., 2005, 2011), partial melting of subducted slab (Defant and Drummond, 1990; Kay, 1978; Kay et al., 1993), low degree partial melting of metasomatized mantle (Gao et al., 2007) or high-pressure fractional crystallization involving garnet (e.g. Macpherson et al., 2006).

### 6.2. Fractionation of amphibole and/or garnet

The chondrite-normalized REE profile of Bibi-Maryam samples displays a slightly concave upward shape. The distribution coefficient of MREEs (middle REEs) relative to HREEs (heavy REE) is higher in amphibole (e. g. Blundy and Wood, 2003) leading to preferential incorporation of MREEs in amphibole relative to HREEs (e.g., Macpherson et al., 2006). An indicator for amphibole fractionation is thus Dy/Yb (Davidson et al., 2007). A second geochemical parameter closely investigated here is La/Yb which is controlled by garnet presence during high-pressure fractionation of hydrous melt, especially for the genesis of adakites and deep-seated fractionation of arc magmas (Castillo et al., 1999; Davidson et al., 2007; Kolb et al., 2013; Macpherson et al., 2006). The positive correlation between Y and $SiO_2$ (Fig. 4) suggests that amphibole fractionation is largely insignificant. This assessment is in agreement with the petrographical observations revealing no amphibole in the samples. The lack of negative and positive trends in Dy/Yb vs. $SiO_2$, and La/Yb vs. $SiO_2$ diagrams, respectively, (Fig. 10) suggests that fractional crystallization including both high-pressure processes (involving garnet fractionation) and low-pressure processes (involving amphibole and without garnet fractionation) is not responsible for the generation of Bibi-Maryam pluton. Therefore, we infer that amphibole and garnet effects on REE fractionation are not due to subsequent fractional crystallization of an intermediate to silicic

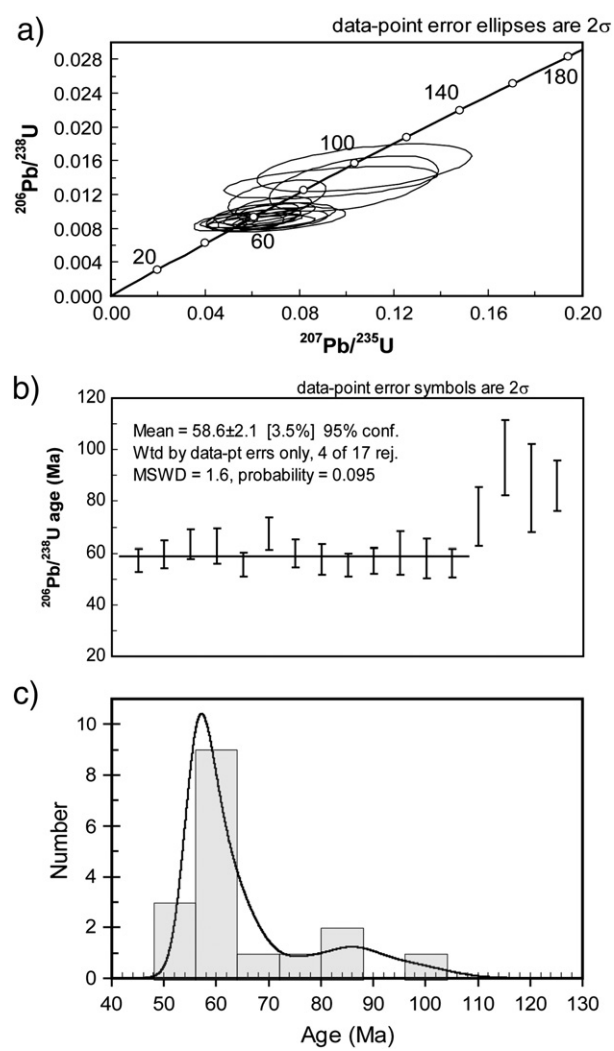


**Fig. 7.** a) Concordia plots of U–Pb age dating results of zircons from Bibi-Maryam pluton. b) $^{206}Pb/^{238}U$ average ages. c) Histograms showing frequency of U–Pb ages.

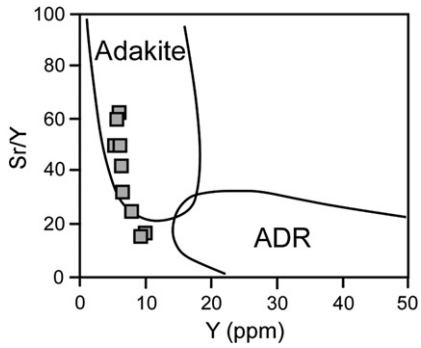


**Fig. 8.** Sr/Y vs. Y diagram (Drummond and Defant, 1990) representing plotting of studied samples within adakite field. ADR is the normal arc andesite, dacite and rhyolite field.

melt but rather as a result of their presence as residual phases in the melt source. In other words, re-melting of garnet and amphibole-bearing rocks in the stability field of these mineral phases is our preferred mechanism to generate the adakitic signature of the Bibi-Maryam plutonic rocks (Guo et al., 2007; Wang et al., 2005).

A caveat for our interpretation of Dy/Yb vs. $SiO_2$ and La/Yb vs. $SiO_2$ diagrams is that accessory minerals such as apatite, sphene or zircon can have a significant influence on relative REE abundances. The lack of $P_2O_5$ and $TiO_2$ depletion with increasing $SiO_2$ variation (not shown), however, suggests minor effects of apatite or sphene fractionation.

### 6.3. Modeling of partial melting

To model the chemical composition of adakitic melts generated by partial melting of subducted slab, we used the average composition of N-MORB-like ophiolitic basalts from the Nehbandan ophiolitic complex (Delavari, 2010; Saccani et al., 2010) as representative of the subducted basaltic portion of oceanic crust in the Sistan Ocean. Eclogitic rocks from the Ratuk complex in the Sulabest area (Angiboust et al., 2013) have also been considered as a model source. The Nehbandan ophiolitic complex contains MORB compositions that are characterized as both

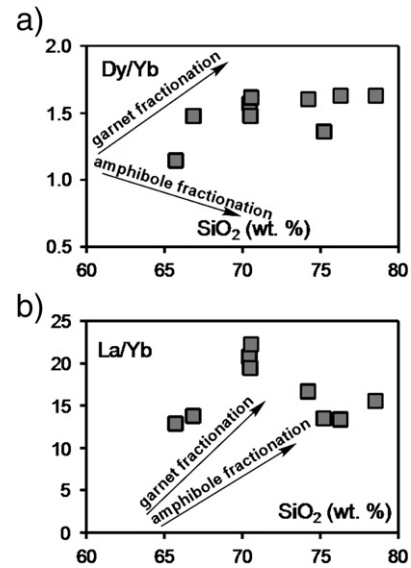


**Fig. 10.** Dy/Yb vs. $SiO_2$ (a) and La/Yb vs. $SiO_2$ (b) diagrams showing the trends of Bibi-Maryam samples in comparison with garnet and amphibole fractionation trends (Davidson et al., 2007).

N- and E-types (Delavari, 2010; Saccani et al., 2010), which also have been detected in the chemistry of Ratuk eclogitic rocks (Angiboust et al., 2013). Hence, we initially also examined E-MORB as a potential melt source, but due to a poor trace element compositional match, we can confidently rule it out, and are not further considering it here. The average composition of Nehbandan ophiolites is similar to global N-MORB averages of Sun and McDonough (1989). Light ion lithophile elements (especially Sr and Ba) in Nehbandan ophiolites, however, differ from typical N-MORB (Sun and McDonough, 1989) possibly due to alteration or fractionation, and we thus use global average values instead in our model. In addition to the basaltic source, a sedimentary component is included in the source based on average trench sediment compositions (Plank and Langmuir, 1998). This is because in many subduction systems the chemistry of arc magmas indicates the

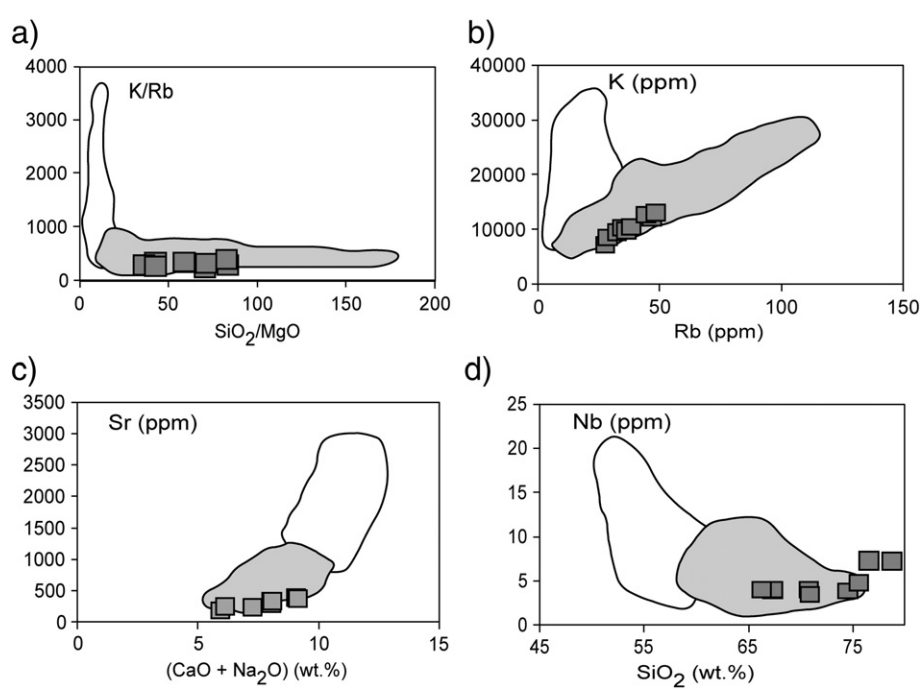


**Fig. 9.** K/Rb vs. $SiO_2$/MgO (a), K vs. Rb (b), Sr vs. CaO + $Na_2O$ (c) and Nb vs. $SiO_2$ diagrams representing the compositional variations of Bibi-Maryam samples compared to high-$SiO_2$ (gray field) and low-$SiO_2$ (light field) adakites. The fields of high-$SiO_2$ and low-$SiO_2$ adakites are from Martin et al. (2005).

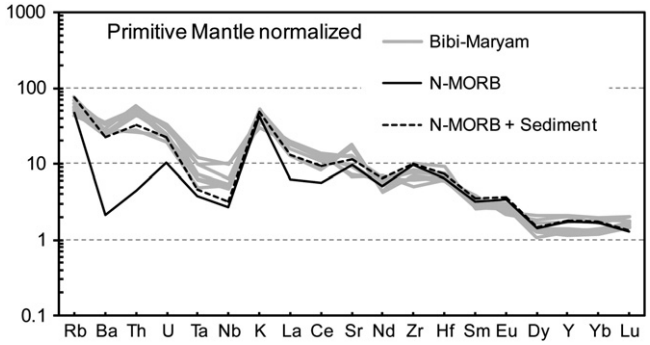


**Fig. 11.** Primitive mantle-normalized (Sun and McDonough, 1989) multi-element patterns for Bibi-Maryam samples and the theoretical adakite melt compositions from assumed N-MORB and N-MORB + sediment sources (Appendix C). See text for more explanation.

involvement of a subducted sediment component (e.g., Gomez-Tuena et al., 2003; Ishizuka et al., 2007; Nebel et al., 2011; Plank and Langmuir, 1998). The model basaltic and sedimentary source compositions are summarized in Appendix C. We consider a source mineralogy of amphibole + clinopyroxene + garnet + apatite + rutile with the following relative contributions of each phase during melting: 60% amphibole + 30% clinopyroxene + 15% apatite + (−10%) garnet + 5% rutile (Guo et al., 2007 and references therein). Partition coefficients are from Klemme et al. (2005); Prowatke and Klemme (2006); Guo et al. (2007), and non-modal batch melting equations are used (Rollinson, 1993; Shaw, 1970). Fig. 11 displays the resulting primitive mantle-normalized trace element patterns for the model melts in comparison with the Bibi-Maryam samples. We examined various mineralogical compositions of the melt source and varied the degree of melting to obtain a model melt composition that matches the range of Bibi-Maryam rock compositions (except for Nb whose model abundances are ~20% lower than actual rock values; Fig. 11). Regardless of this minor discrepancy for Nb, the best model fit was achieved by using the source mineral proportions of 35–40% amphibole + 5–10% garnet + 55–60% clinopyroxene + 1% apatite + 1% rutile and a melt fraction of 5–8%. Fig. 11 also illustrates the two main model melts: one for a pure N-MORB source and the other for a N-MORB + sediment source. Our modeling shows that the trace element profile of the model melt from pure N-MORB source broadly agrees with adakite patterns in terms of some trace element concentrations, but significantly deviates in Ba, Th, U, La and Ce abundances. Adding a low amount of sediment component with the proportion of 95% N-MORB + 5% sediment, however, satisfactorily reproduces Bibi-Maryam adakite trace element patterns (Fig. 11). Comparing two above-mentioned modeling, one of the elements that represents higher variance is Ba, the constituent expected to show higher concentration with sediment portion contribution in melt production (e.g., Defant and Drummond, 1990). Therefore, involvement of sediments in melt production is likely an essential process. Our results are in line with adakite modeling in other subduction zones. High-Sr rock suites in the Kitakami Mountains, Japan, for example, yielded similar mass balance results with a model melt source comprising 95% MORB + 5% sediments and a garnet, clinopyroxene, quartz, rutile and apatite restite (Tsuchiya and Kanisawa, 1994). Other examples include the Mariana arc (Elliot et al., 1997) and Gangdese Belt, southern Tibet (Zhu et al., 2009), where magma chemistry implies a contribution of subducted sediments in melt production.

An important corollary of our model is the presence of amphibole in the melt source. This is indicated by normalized trace element profiles. In primitive mantle-normalized multi-element patterns (Fig. 5b), Ba shows a negative anomaly in comparison with Rb. Because amphibole has a higher partition coefficient for Ba than Rb (Green, 1994; Villemant et al., 1981), this would indicate amphibole-present melt generation.

The comparatively low Nb/Ta in Bibi-Maryam rocks relative to melts derived from rutile-bearing eclogite is another argument hinting at residual amphibole. Compositional fields devised for amphibolite or hornblende eclogite melting have Nb/Ta below the primitive mantle value (~17) (Condie, 2005; Foley et al., 2002). Nb/Ta in Bibi-Maryam samples is mostly <15, consistent with a hornblende eclogite or garnet amphibolite source where amphibole, clinopyroxene and garnet constitute the main minerals.

One potential problem of our model is that the Mg#s of Bibi-Maryam rocks are relatively high (57.1 to 72.3) and in excess of Mg# in experimental melts representing slab melting (Rapp and Watson, 1995; Rapp et al., 1991). We propose that the slab melt interacted with mantle peridotite during melt transition through overlying mantle wedge leading to an increase in Mg# (Martin, 1999; Smithies, 2000). High Mg# is thus not in contrast with our slab melting model. Although, high Mg# may provide a significant constraint for the origin of melt from the thickened lower crust. In the Andean Austral Volcanic Zone, the adakitic rocks are characterized by high Mg# and Stern and Kilian (1996), based on major and trace elements and isotopic evidence argue that high Mg# is in conflict with melting of mafic lower crust. But instead, they referred this chemical feature to the melt source from subducted oceanic basalt recrystallized to garnet-amphibolite or eclogite and melt interaction with overlying mantle wedge.

## 7. Geotectonic framework

### 7.1. Constraints on the lifetime of the Sistan Ocean

Previous studies diverge strongly regarding the proposed evolution of the Sistan ocean (e.g., Angiboust et al., 2013; Babazadeh and de Wever, 2004; Bröcker et al., 2013; Camp and Griffis, 1982; Delavari et al., 2009; Desmons and Beccaluva, 1983; Fotoohi Rad et al., 2005; Pang et al., 2012, 2013; Saccani et al., 2010; Tirrul et al., 1983; Zarrinkoub et al., 2012). A major limitation thus far has been inadequate geochronology for the Sistan suture zone, and therefore our new results bear directly on some of the proposed scenarios for the geodynamic evolution of the Sistan oceanic basin. Zircon U–Pb ages from two leucogabbros of Birjand ophiolite of 113 ± 1 and 107 ± 1 Ma suggest ophiolite formation in the mid-Cretaceous (Zarrinkoub et al., 2012). Moreover, Babazadeh and De Wever (2004) reported Aptian and Albian (Early Cretaceous) radiolarites from the Gazik area in the northern part of the Sistan suture zone, whereas Rb–Sr and Ar–Ar ages of Bröcker et al. (2013) range between 83 and 87 Ma for high-pressure–low temperature metamorphic rocks in the eastern part of the Sistan suture zone. These findings are in conflict with the result of previous investigations proposing that the Sistan Ocean formed as a short-lived oceanic basin whose opening post-dates the upper Cretaceous (Camp and Griffis, 1982; Tirrul et al., 1983). Equally controversial is when the Sistan oceanic basin closed. Tirrul et al. (1983) and Camp and Griffis (1982) pointed out that ophiolite was emplaced during the Late Cretaceous but continental collision resulting in the complete closure of the Sistan ocean occurred only in the Eocene. Likewise, Dercourt et al. (1986) claimed a post-Cretaceous age (Priabonian–Oligocene) for the Sistan ocean closure. In contrast, Zarrinkoub et al. (2010) on the basis of 71–86 Ma ages for adakitic granodiorite favored ocean closure by the Late Cretaceous (>86 Ma). In addition, Pang et al. (2013) using trace element and Sr–Nd isotopic features of Eocene–Oligocene magmatic rocks in the Lut–Sistan region, suggest a scenario in which these magmatic associations are post-collisional and the continental collision could have been occurred in Late Cretaceous to Late Paleocene times (~86–55 Ma).

### 7.2. Evidence of thickened continental crust vs. intra-oceanic arc settings

Zarrinkoub et al. (2010) described granodiorite intrusions with adakitic affinity with ages of 86–71 Ma. According to their model, these adakitic rocks are post-collisional and thus likely products of partial melting of thickened lower crust. This would place the collision between the Lut and Afghan continental blocks in the Late Cretaceous (i.e., predating 86 Ma). If continental collision and crustal thickening

indeed predated ~86 Ma, melting of thickened lower crust in the garnet stability field could be an alternative viable option for the genesis of adakites in the Sistan suture zone. In this case, crustal thickening could have progressed through magmatic underplating in a magmatic arc and tectonic shorting with the overriding continental plate. Modern examples for adakite genesis in thickened continental crust include Cordillera Blanca Batholith in the Central Andes where Na-rich adakitic melts have been attributed to originating from underplated basaltic crust (Petford and Atherton, 1996). The model of Petford and Atherton (1996) includes two stages: first, partial melting in upper mantle creating mafic underplating followed by partial melting of underplated intrusions below thick continental crust at depths within the garnet stability field (>40 km). In this scenario, the residual mineralogy mostly consists of garnet, clinopyroxene and amphibole and can generate leucogranodiorites with an adakitic signature. In the Peruvian Andes, Coldwell et al. (2011) proposed a similar process for adakitic rocks as partial melting of garnet-bearing hydrous mafic lower crust along with lesser extent crustal contamination. In the Lhasa terrane adakitic melts have been linked to partial melting of lower crust in post-collisional tectonic setting where the crust is >70 km in thickness (Guo et al., 2007). For the Macuchi arc, Western Cordillera, Ecuador, Chiaradia (2009) postulated that intermediate to silicic adakitic rocks were originated from mantle magma evolution within lower to mid-crustal level of a thickened arc crust.

In the case of the Bibi-Maryam rocks, we dismiss such a scenario. We argue that the Bibi-Maryam pluton formed in a subduction zone because it is entirely contained within ophiolitic suture zone rocks, and it has no apparent relation with adjacent continental margins. Granitic rock types within ophiolites worldwide (Li and Li, 2003) include (1) plagiogranites, (2) anatectic melts from amphibolites in high-temperature shear zones (at relatively low pressures), (3) obduction-type granites originating from anatectic melts of sedimentary rocks in thrust sheets during ophiolite obduction, and (4) subduction-type granites relating to dehydration melting of the upper oceanic lithosphere in the garnet and amphibole stability field during subduction. Type (4) includes typical adakites (Defant and Drummond, 1990). Geochemically, the Bibi-Maryam pluton is distinct from Type (1) plagiogranites in terms of major and trace element geochemistry (e.g. Floyd et al., 1998). Furthermore, shear- and obduction-type granites commonly represent low Mg# (<50) rocks with a distinct Sr negative anomaly (Li and Li, 2003). This is in contrast to Bibi-Maryam plutonic compositions, and thus types (2) and (3) can reasonably be discounted as models for Bibi-Maryam.

Furthermore, geological evidence suggests that the Lut–Afghan continental collision did probably not happen before the Eocene (Arjmandzadeh et al., 2011; Camp and Griffis, 1982; McCall, 1997; Sengör et al., 1988; Tirrul et al., 1983). Maastrichtian pelagic microfaunal age from the ophiolitic associations of the Sistan suture zone (Tirrul et al., 1983) implies that the time life of the Sistan Ocean extended into the Late Cretaceous. Also, Tirrul et al. (1983) provided stratigraphical and structural evidence suggesting that compression in the Sistan suture zone persisted during middle Eocene and younger times. This includes emergence of the Sistan belt and folding of the Sefidabeh basin deposits, which Tirrul et al. (1983) interpreted as the result of the Lut–Afghan continental blocks collision. Moreover, McCall (1997) argued that the flysch sequences reaching up to ten thousand or more meters in thickness in Saravan and Narreh-Now quadrangles show that the Sistan Ocean remained open during Eocene. Another line of evidence is intrusive rocks with an adakitic signature and ages of 33–34 Ma in the Lut block which were interpreted as the result of melting of a metasomatized mantle source above an active down-going slab of the Sistan ocean (Arjmandzadeh et al., 2011). In addition, the geological features from other parts of the suture around CEIM could be useful. However, the spatial extent and continuity of oceanic seaway around CEIM is subject of debate. In this regard, two hypotheses could be assumed: 1) the north-western termination of the Sistan suture zone represents no connection with Sabzevar suture confirming no linkage between the Sistan and Sabzevar oceanic basins (Tirrul et al., 1983); 2) the Sabzevar and Sistan oceans were once-continuous basin (e.g. Dercourt et al., 1986; Rossetti et al., 2010; Şengör, 1990; Sengör et al., 1988) or as sectors of a ring ocean surrounding CEIM (McCall, 1997). Considering the second alternative, it would be reasonable to expect some tectono-magmatic similarities between these two basins. In the Sabzevar area, Rossetti et al. (2014) believe that the Sabzevar Ocean shortly closed after its formation via subduction of a young oceanic lithosphere and the ending of Sabzevar subduction and subsequent continental collision happened during the Paleocene–Eocene which is contemporaneous to the closure of other marginal basins around CEIM (McCall and Kidd, 1982). Accordingly, Omrani et al. (2013) studied the formation of Sabzevar metamorphic rocks and interpreted them as the products of north-east-dipping subduction of Sabzevar ocean which finally led to oceanic closure during lower Eocene. This is consistent with K-Ar and Rb-Sr dating of granitic rocks in the range of 51–53 Ma and K–Ar dating of amphibolite-gneissic rocks ranging from 51 to 54 Ma revealing tectono-metamorphic events in Lower Eocene in Sabzevar area (Baroz et al., 1983). From the viewpoint of regional plate tectonic evolution, the closure of the Sistan Ocean could be likely tied to the tectonic movements in southeast Asia due to convergence of India and Asia which caused westerly motion of Afghan continental block (Şengör, 1990; Sengör et al., 1988). Although, the precise timing of initiation of India–Asia collision is not well constrained and remained a subject of considerable debate. Based on many geological investigations conducted in the Himalayan orogen, the collision time shows wide range of estimates varying from late Cretaceous to the end of Eocene (~70 to 34 Ma) for various places along strike of the Himalayan orogen (Aitchison et al., 2007; Dercourt et al., 1986; Ding et al., 2005; Khan et al., 2009; Najman et al., 2001; Rowley, 1996; Treloar and Izatt, 1993; Zhu et al., 2005). Although the evidence of Cretaceous–Tertiary movements between continental blocks such as Lut, Afghan and India are inadequate to allow reconstruction of relative motions between these blocks, it is noteworthy that if we suppose India–Asia collision as a prerequisite for compressional tectonic regime in eastern Iran, then we should expect the Lut–Afghan continental collision in a time after Cretaceous.

Hence, we favor a scenario in which the Sistan Ocean did not close by the Eocene and it contained an intra-oceanic subduction system during the Late Cretaceous. This is supported by mineralogical and geochemical evidence from the Nehbandan ophiolitic complex that indicate an intra-oceanic supra-subduction zone setting. Whole rock and mineral chemistry of crustal ultramafic and mafic cumulates and the geochemical nature of mantle tectonites reveal depleted and re-enriched nature of a mantle wedge evolving in a subduction system (Delavari, 2010; Delavari et al., 2009; Saccani et al., 2010). Supra-subduction geochemical affinity is also evident in parental rocks of high-pressure, low-temperature metabasites within the Sulabest area which resulted from subduction within the Sistan Ocean (Angiboust et al., 2013). Moreover, the highly depleted nature of mantle peridotites within the Birjand ophiolite has been interpreted to result from more than one melt extraction event consistent with mantle evolution in an intra-oceanic arc setting (Zarrinkoub et al., 2012). However, to define an intra-oceanic subduction system, it is important to consider spatial distribution of arc magmatic rocks from a regional perspective. In Sistan suture zone further studies are necessary to clarify the tectonic setting and age of the magmatic association. With the exception of the study of Pang et al. (2013) that provided precise age and geochemical data from magmatic rocks in the Lut–Sistan region (mostly northern part of the Sistan suture zone), this zone, specially, central and southern parts are poorly studied and understood so valid documentation is not possible now. In the study of Camp and Griffis (1982), the linear north–south trend of calk-alkaline suites is presented which are, however, not differentiated in detail based on geochemistry and age. Based on Camp and Griffis (1982) pre-collision magmatism was dominated by a Cretaceous–Paleocene calc-alkaline volcanism ($KP^v$ unit) which they interpreted it

as product of early stages in the development of an incipient island-arc and we think it could be an equivalent magmatic activity to Bibi-Maryam adakite in arc setting. In this case, the subducted slab can be melted which require an unusual hot thermal regime to intersect wet basalt solidus (e.g. Peacock et al., 1994). In this respect, many workers pointed out the subduction of young (<25 Ma) oceanic crust (Defant and Drummond, 1990; Drummond and Defant, 1990). Likewise, in the Sabzevar Range at the northern border of the CEIM, Rossetti et al. (2014) reported a suite of granitoid intrusives with adakitic affinity emplaced within ophiolitic suture zone of the Sabzevar. Based on U–Pb zircon and $^{40}Ar/^{39}Ar$ white mica and amphibole geochronology they have revealed that the age of Sabzevar magmatism is late Paleocene (ca. 58 Ma) which is quite similar to the age of Bibi-Maryam adakite. Furthermore, the generation of Sabzevar adakitic suite was interpreted as the result of partial melting of metamorphosed portion (garnet amphibolite) of hot subducted oceanic slab and subsequent magma differentiation and high-pressure amphibole fractionation.

Although, it should be noted that the subduction of young and relatively hot oceanic slab due to its buoyancy is ambiguous. There are, however, alternative scenarios that permit melting of the slab crust irrespective of the age of subducted slab. A modern example is the Philippine Sea where old (>50 Ma) oceanic lithosphere subducted beneath Mindanao and generated adakitic melts (Macpherson et al., 2006). In this case, young subduction instead of a young and hot slab is crucial for generating Mindanao adakites where the leading edge of the subducted slab can heat above its solidus temperature (Sajona et al., 1993). Alternatively, Macpherson et al. (2006) suggested high-pressure differentiation of island arc magma originating from fluid-modified mantle for Mindanao adakites. In contrast to the models which require a thickened crust to stabilize garnet for the source of adakitic melt, Macpherson et al. (2006) discuss adakite genesis beneath an arc with thin crust and high pressure crystallization of basaltic arc magma at mantle depths. In this model direct high-pressure differentiated liquid or indirect re-melting of solidified materials could produce adakitic melts.

Regardless of the melt origin, it is likely that thick continental crust would modify the composition of ascending melts, so, it is widely expected that the magmatic rocks involving crustal materials are more enriched in large ion lithophile elements. This would especially affect the abundances of incompatible elements enriched in continental crust such as $K_2O$, Rb, Ba, Cs, U and Th (e.g., Drummond et al., 1996; Esperanca et al., 1992; Kay et al., 1993), and consequently adakites

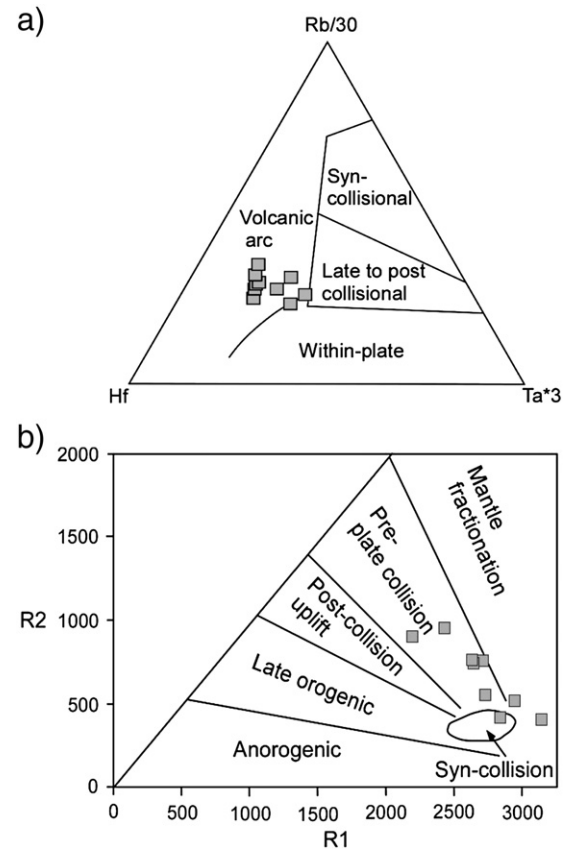


**Fig. 13.** a) Rb/30–Hf–Ta*3 diagram (Harris et al., 1986). b) R1–R2 diagram with geotectonic implications (Batchelor and Bowden, 1985). R1 = 4Si − 11 (Na + K) − 2 (Fe + Ti); R2 = 6Ca + 2 Mg + Al.

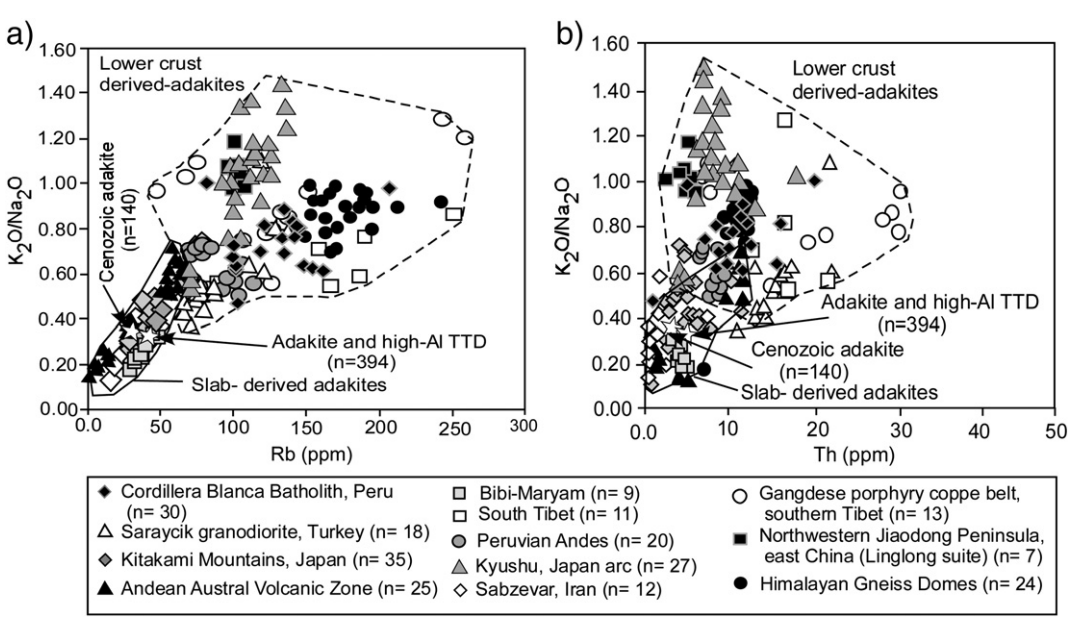


**Fig. 12.** a) $K_2O/Na_2O$ vs. Rb (a) and $K_2O/Na_2O$ vs. Th (b) diagrams for Bibi-Maryam pluton. The value of n shows the number of samples. Comparative data for lower crust-derived adakites are from Petford and Atherton (1996) (Cordillera Blanca Batholith, Peru), Topuz et al. (2005) (Saraycik granodiorite, Turkey), Guo et al. (2007) (South Tibet), Coldwell et al. (2011) (Peruvian Andes), Kamei et al.(2009) (Kyushu, Japan arc), Li et al. (2011) (Gangdese porphyry copper belt, southern Tibet), Hou et al. (2007) (northwestern Jiaodong Peninsula, east China), Zeng et al. (2011) (Himalayan Gneiss Domes) and the data of slab-derived adakites are from Tsuchiya et al. (2007) (Kitakami Mountains, Japan), Stern and Kilian (1996) (Andean Austral Volcanic Zone) and Rossetti et al. (2014) (Sabzevar, Iran). The data of adakite and high-Al TTD (trondhjemite–tonalite–dacite) and Cenozoic adakites are from Drummond et al. (1996).

originating from partial melting of thickened lower crust are characteristically enriched in these elements relative to slab-related adakites (e.g. Coldwell et al., 2011; Guo et al., 2007; Hou et al., 2004, 2007; Kamei et al., 2009; Li et al., 2011; Petford and Atherton, 1996; Topuz et al., 2005, 2011; Wang et al., 2005; Zeng et al., 2011). For example, in comparison with Cenozoic slab-derived adakites, some continental arc magmatic associations in Andes representing adakite-like geochemical signatures (e.g., Petford and Atherton, 1996) show higher contents of Rb and $K_2O$, therefore, these elements could discriminate between the slab and lower crustal derivations (Drummond et al., 1996). Accordingly, in the case of Bibi-Maryam adakite, high $Na_2O/K_2O$ and low $K_2O$, Rb and Th values are inconsistent with major continental crustal contamination, or melting within a thickened lower crust. Instead, in terms of these elements, there is good agreement between Bibi-Maryam adakite and those thought to have resulted from slab melting (e. g. Rossetti et al., 2014; Stern and Kilian, 1996; Tsuchiya et al., 2007; Tsuchiya and Kanisawa, 1994) (Fig. 12a,b). Geochemical evidence thus suggests that the Bibi-Maryam adakite has formed in an oceanic arc setting prior to crustal thickening resulting from Sistan suture zone continental collision (Figs. 13a,b). This implies that the collision of the Lut–Afghan continental blocks postdates the emplacement of the Bibi-Maryam rocks at about 58.6 ± 2.1 Ma.

## 8. Conclusion

U–Pb zircon geochronology and major and trace element geochemistry presented in this study allow us to develop a new tectonic model for the evolution of the Sistan suture zone. The Bibi-Maryam pluton is a high $Na_2O/K_2O$ leucogranitoid with adakitic affinity. U–Pb zircon ages indicate a Paleocene (58.6 ± 2.1 Ma) age. Geochemical characteristics (low $K_2O$, Rb and Th) indicate that the Bibi-Maryam adakite is dissimilar to adakites generated by partial melting in overthickened continental crust. Also, crystal fractionation of garnet and amphibole is not detected in trace element modeling of Bibi-Maryam adakite. Instead, trace element modeling is consistent with adakitic melts produced by ~5–8% partial melting from N-MORB basaltic with a minor sedimentary component. This could have occurred in the upper part of a subducted slab in the field of amphibolite/eclogite facies which subsequently hybridized with mantle peridotites during ascent through the mantle wedge. Therefore, combining geochronological, mineralogical and geochemical data from this study with field data from the literature suggest that the Bibi-Maryam pluton formed in an intra-oceanic subduction system prior to crustal thickening of the Lut–Afghan continental blocks collision. This implies that the closure of the Sistan ocean postdates the Paleocene.

## Acknowledgments

The ion microprobe facility at UCLA is partly supported by a grant from the Instrumentation and Facilities Program, Division of Earth Sciences, National Science Foundation (award numbers 1029193 and 1339051). The University of Kharazmi is acknowledged for the financial support for fieldworks and analyzing some whole-rock samples. We are very grateful to Emilio Saccani and Kwan-Nang Pang for their careful and constructive reviews.

## Appendix A

Representative analyses of biotite from the Bibi-Maryam pluton. Calculations based on 22 anion and 16 cation.

| Sample | MD2-42 | MD2-42 | MD2-42 | MD2-42 | MD2-42 | MD2-42 | MD4-26 | MD4-26 | MD4-27 | MD4-27 | MD4-27 |
|---|---|---|---|---|---|---|---|---|---|---|---|
| Point | 1 | 2 | 20 | 27 | 41 | 42 | 73 | 74 | 87 | 88 | 89 |
| $SiO_2$ | 34.50 | 34.83 | 35.46 | 34.40 | 34.35 | 34.96 | 35.27 | 34.58 | 35.04 | 34.97 | 36.21 |
| $TiO_2$ | 1.71 | 1.77 | 1.88 | 1.80 | 2.12 | 2.20 | 1.71 | 1.26 | 1.77 | 1.68 | 1.95 |
| $Al_2O_3$ | 18.88 | 18.58 | 17.89 | 18.36 | 19.50 | 19.46 | 18.98 | 18.36 | 18.43 | 18.40 | 18.38 |
| $Cr_2O_3$ | 0.00 | 0.00 | 0.05 | 0.00 | 0.04 | 0.05 | 0.00 | 0.05 | 0.02 | 0.00 | 0.03 |
| FeO | 17.99 | 17.51 | 17.74 | 18.55 | 18.60 | 18.35 | 17.38 | 18.62 | 17.39 | 17.20 | 17.44 |
| MnO | 0.64 | 0.56 | 0.52 | 0.51 | 0.63 | 0.65 | 0.41 | 0.48 | 0.45 | 0.49 | 0.52 |
| MgO | 11.00 | 11.10 | 11.84 | 12.29 | 10.46 | 10.82 | 11.85 | 12.48 | 12.01 | 12.07 | 12.03 |
| CaO | 0.01 | 0.11 | 0.01 | 0.06 | 0.01 | 0.11 | 0.02 | 0.03 | 0.00 | 0.00 | 0.01 |
| $Na_2O$ | 0.17 | 0.22 | 0.15 | 0.18 | 0.19 | 0.22 | 0.13 | 0.09 | 0.14 | 0.15 | 0.15 |
| $K_2O$ | 9.69 | 8.75 | 9.81 | 8.31 | 9.55 | 9.16 | 9.82 | 9.51 | 9.99 | 9.92 | 10.11 |
| Total | 94.57 | 93.42 | 95.35 | 94.46 | 95.44 | 95.96 | 95.56 | 95.47 | 95.23 | 94.89 | 96.80 |
| Si | 5.297 | 5.368 | 5.389 | 5.264 | 5.235 | 5.272 | 5.328 | 5.270 | 5.329 | 5.333 | 5.403 |
| Ti | 0.198 | 0.206 | 0.215 | 0.207 | 0.243 | 0.249 | 0.194 | 0.145 | 0.202 | 0.193 | 0.219 |
| Al | 3.416 | 3.375 | 3.204 | 3.311 | 3.502 | 3.459 | 3.380 | 3.297 | 3.303 | 3.307 | 3.232 |
| Cr | 0.000 | 0.000 | 0.006 | 0.000 | 0.004 | 0.006 | 0.000 | 0.006 | 0.002 | 0.000 | 0.003 |
| $Fe^{2+}$ | 2.311 | 2.257 | 2.255 | 2.373 | 2.371 | 2.315 | 2.196 | 2.374 | 2.211 | 2.194 | 2.176 |
| Mn | 0.083 | 0.073 | 0.067 | 0.066 | 0.082 | 0.083 | 0.052 | 0.062 | 0.058 | 0.063 | 0.066 |
| Mg | 2.518 | 2.550 | 2.682 | 2.804 | 2.375 | 2.433 | 2.669 | 2.836 | 2.722 | 2.744 | 2.676 |
| Ca | 0.002 | 0.018 | 0.002 | 0.010 | 0.001 | 0.017 | 0.003 | 0.005 | 0.000 | 0.000 | 0.001 |
| Na | 0.049 | 0.065 | 0.043 | 0.054 | 0.056 | 0.063 | 0.037 | 0.027 | 0.041 | 0.046 | 0.042 |
| K | 1.898 | 1.720 | 1.903 | 1.621 | 1.857 | 1.762 | 1.892 | 1.849 | 1.939 | 1.930 | 1.924 |
| Total | 15.771 | 15.631 | 15.764 | 15.711 | 15.725 | 15.659 | 15.752 | 15.872 | 15.806 | 15.809 | 15.743 |
| Mg/(Fe + Mg) | 0.52 | 0.53 | 0.54 | 0.54 | 0.50 | 0.51 | 0.55 | 0.54 | 0.55 | 0.56 | 0.55 |

## Appendix B

Representative analyses of plagioclase from Bibi-Maryam pluton. Ab: albite; An: anorthite; Or: orthoclase. Calculations based on 8 anion and 5 cation.

| Sample | MD4-26 | MD4-26 | MD4-26 | MD4-27 | MD4-27 | MD4-27 | MD4-27 | MD4-42 | MD4-42 | MD4-44 | MD4-44 | MD4-44 | MD4-28 | MD4-28 | MD4-28 | MD4-28 | MD4-28 |
|---|---|---|---|---|---|---|---|---|---|---|---|---|---|---|---|---|---|
| Point | 97 | 101 | 103 | 107 | 108 | 110 | 112 | 122 | 124 | 125 | 126 | 127 | 186 | 187 | 188 | 189 | 192 |
| $SiO_2$ | 54.18 | 55.94 | 62.23 | 54.46 | 58.10 | 59.41 | 61.13 | 60.41 | 58.37 | 60.21 | 60.28 | 54.24 | 62.23 | 55.58 | 57.32 | 58.56 | 59.83 |
| $TiO_2$ | 0.00 | 0.00 | 0.00 | 0.02 | 0.00 | 0.00 | 0.00 | 0.00 | 0.00 | 0.03 | 0.01 | 0.00 | 0.00 | 0.03 | 0.01 | 0.02 | 0.02 |
| $Al_2O_3$ | 29.06 | 27.90 | 22.94 | 29.13 | 26.14 | 25.79 | 24.34 | 23.78 | 26.04 | 24.56 | 24.56 | 28.03 | 22.99 | 27.43 | 26.17 | 25.28 | 24.50 |
| $Cr_2O_3$ | 0.00 | 0.00 | 0.00 | 0.03 | 0.01 | 0.00 | 0.01 | 0.00 | 0.00 | 0.00 | 0.04 | 0.00 | 0.00 | 0.00 | 0.00 | 0.00 | 0.00 |

**Appendix B** (*continued*)

| Sample | MD4-26 | MD4-26 | MD4-26 | MD4-27 | MD4-27 | MD4-27 | MD4-27 | MD4-42 | MD4-42 | MD4-44 | MD4-44 | MD4-44 | MD4-28 | MD4-28 | MD4-28 | MD4-28 | MD4-28 |
|---|---|---|---|---|---|---|---|---|---|---|---|---|---|---|---|---|---|
| Point | 97 | 101 | 103 | 107 | 108 | 110 | 112 | 122 | 124 | 125 | 126 | 127 | 186 | 187 | 188 | 189 | 192 |
| FeO | 0.03 | 0.03 | 0.07 | 0.05 | 0.04 | 0.05 | 0.02 | 0.07 | 0.03 | 0.17 | 0.20 | 0.02 | 0.04 | 0.09 | 0.03 | 0.00 | 0.03 |
| MnO | 0.02 | 0.05 | 0.04 | 0.00 | 0.03 | 0.00 | 0.00 | 0.01 | 0.03 | 0.05 | 0.01 | 0.04 | 0.00 | 0.01 | 0.00 | 0.00 | 0.00 |
| MgO | 0.00 | 0.03 | 0.00 | 0.00 | 0.00 | 0.02 | 0.00 | 0.00 | 0.00 | 0.00 | 0.02 | 0.00 | 0.01 | 0.00 | 0.02 | 0.00 | 0.00 |
| CaO | 10.45 | 9.15 | 3.37 | 10.39 | 7.28 | 6.08 | 4.83 | 4.67 | 6.68 | 5.26 | 5.28 | 9.89 | 3.42 | 8.60 | 7.36 | 6.34 | 5.42 |
| $Na_2O$ | 5.60 | 6.33 | 9.69 | 5.59 | 7.52 | 8.37 | 8.74 | 8.82 | 7.74 | 8.74 | 8.74 | 5.79 | 9.78 | 6.59 | 7.46 | 7.99 | 8.89 |
| $K_2O$ | 0.08 | 0.10 | 0.17 | 0.09 | 0.09 | 0.20 | 0.17 | 0.26 | 0.19 | 0.12 | 0.13 | 0.10 | 0.15 | 0.15 | 0.14 | 0.17 | 0.11 |
| Total | 99.42 | 99.53 | 98.49 | 99.76 | 99.22 | 99.91 | 99.22 | 98.01 | 99.08 | 99.13 | 99.27 | 98.10 | 98.61 | 98.48 | 98.50 | 98.35 | 98.81 |
| Si | 2.456 | 2.524 | 2.794 | 2.460 | 2.616 | 2.652 | 2.731 | 2.736 | 2.629 | 2.703 | 2.702 | 2.489 | 2.791 | 2.534 | 2.603 | 2.655 | 2.696 |
| Ti | 0.000 | 0.000 | 0.000 | 0.001 | 0.000 | 0.000 | 0.000 | 0.000 | 0.000 | 0.001 | 0.000 | 0.000 | 0.000 | 0.001 | 0.000 | 0.001 | 0.001 |
| Al | 1.553 | 1.484 | 1.214 | 1.551 | 1.388 | 1.357 | 1.282 | 1.269 | 1.382 | 1.299 | 1.298 | 1.516 | 1.215 | 1.474 | 1.401 | 1.350 | 1.301 |
| Cr | 0.000 | 0.000 | 0.000 | 0.001 | 0.000 | 0.000 | 0.000 | 0.000 | 0.000 | 0.000 | 0.001 | 0.000 | 0.000 | 0.000 | 0.000 | 0.000 | 0.000 |
| $Fe^{2+}$ | 0.001 | 0.001 | 0.002 | 0.002 | 0.002 | 0.002 | 0.001 | 0.003 | 0.001 | 0.006 | 0.008 | 0.001 | 0.002 | 0.004 | 0.001 | 0.000 | 0.001 |
| Mn | 0.001 | 0.002 | 0.001 | 0.000 | 0.001 | 0.000 | 0.000 | 0.000 | 0.001 | 0.002 | 0.000 | 0.001 | 0.000 | 0.000 | 0.000 | 0.000 | 0.000 |
| Mg | 0.000 | 0.002 | 0.000 | 0.000 | 0.000 | 0.001 | 0.000 | 0.000 | 0.000 | 0.000 | 0.001 | 0.000 | 0.001 | 0.000 | 0.001 | 0.000 | 0.000 |
| Ca | 0.508 | 0.442 | 0.162 | 0.503 | 0.351 | 0.291 | 0.231 | 0.227 | 0.322 | 0.253 | 0.253 | 0.486 | 0.164 | 0.420 | 0.358 | 0.308 | 0.262 |
| Na | 0.492 | 0.554 | 0.844 | 0.490 | 0.657 | 0.724 | 0.757 | 0.774 | 0.676 | 0.761 | 0.759 | 0.515 | 0.851 | 0.582 | 0.656 | 0.702 | 0.777 |
| K | 0.005 | 0.006 | 0.010 | 0.005 | 0.005 | 0.012 | 0.009 | 0.015 | 0.011 | 0.007 | 0.007 | 0.006 | 0.009 | 0.009 | 0.008 | 0.010 | 0.007 |
| Total | 5.016 | 5.014 | 5.026 | 5.012 | 5.020 | 5.038 | 5.011 | 5.024 | 5.023 | 5.031 | 5.031 | 5.014 | 5.031 | 5.024 | 5.029 | 5.026 | 5.044 |
| Ab % | 49.0 | 55.3 | 83.1 | 49.1 | 64.8 | 70.6 | 75.9 | 76.2 | 67.0 | 74.5 | 74.4 | 51.1 | 83.1 | 57.6 | 64.2 | 68.8 | 74.3 |
| An % | 50.5 | 44.2 | 16.0 | 50.4 | 34.7 | 28.3 | 23.2 | 22.3 | 32.0 | 24.8 | 24.8 | 48.3 | 16.0 | 41.5 | 35.0 | 30.2 | 25.1 |
| Or % | 0.5 | 0.6 | 0.9 | 0.5 | 0.5 | 1.1 | 0.9 | 1.5 | 1.1 | 0.7 | 0.7 | 0.6 | 0.8 | 0.8 | 0.8 | 1.0 | 0.6 |

## Appendix C

The assumed MORB and sedimentary source compositions used in trace element modeling.

| Sources | Rb | Ba | Th | U | Ta | Nb | K | La | Ce | Sr |
|---|---|---|---|---|---|---|---|---|---|---|
| N-MORB | 5 | 6.3 | 0.08 | 0.04 | 0.13 | 2.1 | 4671 | 1.82 | 6.1 | 90 |
| Sediment | 63 | 1200 | 10 | 1 | 0.693 | 10 | 19094 | 40 | 81 | 422 |

| Sources | Nd | Zr | Hf | Sm | Eu | Dy | Y | Yb | Lu |
|---|---|---|---|---|---|---|---|---|---|
| N-MORB | 5.81 | 74 | 1.27 | 2.13 | 0.7 | 3.903 | 25.8 | 2.272 | 0.326 |
| Sediment | 33 | 149 | 4.5 | 8 | 1.5 | 6.8 | 39 | 3.9 | 0.54 |

## References


Aitchison, J.C., Ali, J.R., Davis, A.M., 2007. When and where did India and Asia collide? Journal of Geophysical Research 112, B05423. http://dx.doi.org/10.1029/2006JB004706.

Alavi, M., 1994. Tectonics of the Zagros Orogenic belt of Iran: new data and interpretations. Tectonophysics 229, 211–238.

Alavi Naini, M., Eftekharnezhad, J., Aghanabati, A., 1990. Geological map of Zabol. Scale 1/250000. Geological survey of Iran.

Allahyari, K., Saccani, E., Pourmoafi, M., Beccaluva, L., Masoudi, F., 2010. Petrology of mantle peridotites and intrusive mafic rocks from the Kermanshah ophiolitic complex (Zagros belt, Iran): implications for the geodynamic evolution of the Neo-Tethyan oceanic branch between Arabia and Iran. Ofioliti 35, 71–90.

Allahyari, K., Saccani, E., Rahimzadeh, B., Zeda, O., 2014. Mineral chemistry and petrology of highly magnesian ultramafic cumulates from the Sarve-Abad (Sawlava) ophiolites (Kurdistan, NW Iran): new evidence for boninitic magmatism in intra-oceanic fore-arc setting in the Neo-Tethys between Arabia and Iran. Journal of Asian Earth Sciences 79, 312–328.

Angiboust, S., Agard, P., De Hoog, J.C.M., Omrani, J., Plunder, A., 2013. Insights on deep, accretionary subduction processes from the Sistan ophiolitic "mélange" (Eastern Iran). Lithos 156, 139–158.

Arjmandzadeh, R., Karimpour, M.H., Mazaheri, S.A., Santos, J.F., Medina, J.M., Homam, S.M. , 2011. Sr-Nd isotope geochemistry and petrogenesis of the Chah-Shaljami granitoids (Lut Block, Eastern Iran). Journal of Asian Earth Sciences 41, 283–296.

Arvin, M., Robinson, P.T., 1994. The petrogenesis and tectonic setting of lavas from the Baft ophiolitic mélange, southwest of Kerman, Iran. Canadian Journal of Earth Sciences 31, 824–834.

Babaie, H.A., Babaei, A., Ghazi, A.M., Arvin, M., 2006. Geochemical, $^{40}Ar/^{39}Ar$ age, and isotopic data for crustal rocks of the Neyriz ophiolite, Iran. Canadian Journal of Earth Sciences 43, 57–70.

Babazadeh, S.A., De Wever, P., 2004. Early Cretaceous radiolarian assemblages from radiolarites in the Sistan Suture (eastern Iran). Geodiversitas 26, 185–206.

Bagheri, S., Stampfli, G.M., 2008. The Anarak, Jandaq and Posht-e-Badam metamorphic complexes in central Iran: new geological data, relationships and tectonic implications. Tectonophysics 451, 123–155.

Baroz, R., Macaudiere, J., Montigny, R., Noghreyan, H., Ohnenstetter, M., Rocci, G., 1983. Ophiolites and related formations in the central part of the Sabzevar range (Iran) and possible geotectonic reconstructions. Geodynamic Project (Geotraverse) in Iran p. 519 (report no. 51).

Batchelor, B., Bowden, P., 1985. Petrogenetic interpretation of granitoid rock series using multicationic parameters. Chemical Geology 48, 43–55.

Berberian, M., King, G.C.P., 1981. Towards a paleogeography and tectonic evolution of Iran. Canadian Journal of Earth Sciences 18, 210–265.

Bird, P., Toksöz, M.N., Sleep, N.H., 1975. Thermal and mechanical models of continent–continent convergence zones. Journal of Geophysical Research 80, 4405–4416.

Blundy, J., Wood, B., 2003. Partitioning of trace elements between crystals and melts: Earth and Planetary Science Letters 210, 383–397.

Bröcker, M., Fotoohi Rad, G., Burgess, R., Theunissen, S., Paderin, I., Rodionov, N., Salimi, Z., 2013. New age constraints for the geodynamic evolution of the Sistan Suture Zone, eastern Iran. Lithos 170–171, 17–34.

Camp, V.E., Griffis, R.J., 1982. Character, genesis and tectonic setting of igneous rocks in the Sistan suture zone, eastern Iran. Lithos 15, 221–239.

Castillo, P.R., Janney, P.E., Solidum, R.U., 1999. Petrology and geochemistry of Camiguin Island, southern Philippines: insights into the source of adakite and other lavas in a complex arc tectonic setting. Contributions to Mineralogy and Petrology 134, 33–51.

Castillo, P.R., 2012. Adakite petrogenesis. Lithos 134–135, 304–316.

Chiaradia, M., 2009. Adakite-like magmas from fractional crystallization and melting-assimilation of mafic lower crust (Eocene Macuchi arc, Western Cordillera, Ecuador). Chemical Geology 265, 468–487.

Chung, S.L., Liu, D., Ji, J., Chu, M.F., Lee, H.Y., Wen, D.J., Lo, C.H., Lee, T.Y., Qian, Q., Zhang, Q., 2003. Adakites from continental collision zones: melting of thickened lower crust beneath southern Tibet. Geology 31, 1021–1024.

Coldwell, B., Clemens, J., Petford, N., 2011. Deep crustal melting in the Peruvian Andes: felsic magma generation during delamination and uplift. Lithos 125, 272–286.

Condie, K.C., 2005. TTGs and adakites: are they both slab melts? Lithos 80, 33–44.

Davidson, J., Turner, S., Handley, H., Macpherson, C., Dosseto, A., 2007. Amphibole "sponge" in arc crust? Geology 35, 787–790.

Defant, M.J., Drummond, M.S., 1990. Derivation of some modern arc magmas by melting of young subducted lithosphere. Nature 347, 662–665.

Delaloye, M., Desmons, J., 1980. Ophiolites and mélange terranes in Iran: a geochronological study and its paleotectonic implications. Tectonophysics 68, 83–111.

Delavari, M., Amini, S., Saccani, E., Beccaluva, L., 2009. Geochemistry and petrology of mantle peridotites from the Nehbandan ophiolitic complex, Eastern Iran. Journal of Applied Sciences 9, 2671–2687.

Delavari, M. 2010. Petrology and geochemistry of Nehbandan ophiolitic complex. Unpublished PhD thesis. Tarbiat Moallem University of Tehran. 298 pp. (in Persian).

Dercourt, J., Zonenshain, L.P., Ricou, L.-E., Kazmin, V.G., Le Pichon, X., et al., 1986. Geological evolution of the Tethys Belt from the Atlantic to the Pamirs since the LIAS. Tectonophysics 123, 241–315.

Desmons, J., Beccaluva, L., 1983. Mid-ocean ridge and island-arc affinities in ophiolites from Iran: palaeographic implications. Chemical Geology 39, 39–63.

Ding, L., Kapp, P., Wan, X.Q., 2005. Paleocene–Eocene record of ophiolite obduction and initial India–Asia collision, south central Tibet. Tectonics 24, TC3001. http://dx.doi.org/10.1029/2004TC001729.
Drummond, M.S., Defant, M.J., 1990. A model for trondhjemite–tonalite–dacite genesis and crustal growth via slab melting: Archaean to modern comparisons. Journal of Geophysical Research 95, 21503–21521.
Drummond, M.S., Defant, M.J., Kepezhinskas, P.K., 1996. Petrogenesis of slab-derived trondhjemite–tonalite–dacite/adakite magmas. Transactions of the Royal Society of Edinburgh: Earth Sciences 87, 205–215.
Elliot, T., Plank, T., Zindler, A., White, W., Bourdon, B., 1997. Element transport from slab to volcanic front at the Mariana arc. Journal of Geophysical Research 102, 14991–15019.
Esperanca, S., Crisci, G.M., de Rosa, R., Mazzuoli, R., 1992. The role of the crust in the magmatic evolution of the island Lipari (Aeolian Islands, Italy). Contributions to Mineralogy and Petrology 112, 450–462.
Floyd, P.A., Yaliniz, M.K., Goncuoglu, M.C., 1998. Geochemistry and petrogenesis of intrusive and extrusive ophiolitic plagiogranites, Central Anatolian Crystalline Complex, Turkey. Lithos 42, 225–241.
Foley, S., Tiepolo, M., Vannucci, R., 2002. Growth of early continental crust controlled by melting of amphibolite in subduction zones. Nature 417, 837–840.
Fotoohi Rad, G.R., Droop, G.T.R., Amini, S., Moazzen, M., 2005. Eclogites and blueschists of the Sistan Suture Zone, eastern Iran: a comparison of PT histories from a subduction mélange. Lithos 84, 1–24.
Fotoohi Rad, G.R., Droop, G.T.R., Burgess, R., 2009. Early Cretaceous exhumation of high-pressure metamorphic rocks of the Sistan Suture Zone, eastern Iran. Geological Journal 44, 104–116.
Gao, Y., Hou, Z., Kamber, B.S., Wei, R., Meng, X., Zhao, R., 2007. Adakite-like porphyries from the southern Tibetan continental collision zones: evidence for slab melt metasomatism. Contributions to Mineralogy and Petrology 153, 105–120.
Ghasemi, A., Talbot, C.J., 2006. A new tectonic scenario for the Sanandaj–Sirjan Zone (Iran). Journal of Asian Earth Sciences 26, 683–693.
Gomez-Tuena, A., LaGatta, A.B., Langmuir, C.H., Goldstein, S.L., Ortega-Gutierrez, F., Carrasco-Nunez, G., 2003. Temporal control of subduction magmatism in the eastern Trans-Mexican Volcanic Belt: mantle sources, slab contributions and crustal contamination. Geochemistry, Geophysics, Geosystems 4. http://dx.doi.org/10.1029/2003GC000524.
Green, T.H., 1994. Experimental studies of trace-element partitioning applicable to igneous petrogenesis-Sedona 16 years later. Chemical Geology 117, 1–36.
Guillou, Y., Maurizot, P., Vaslet, D., Villéon, H., 1983. Geological map of Gazik. Scale 1/250000. Geological survey of Iran.
Guo, Z., Wilson, M., Liu, J., 2007. Post-collisional adakites in south Tibet: products of partial melting of subduction-modified lower crust. Lithos 96, 205–224.
Harris, N.B.W., Pearce, J.A., Tindle, A.G., 1986. Geochemical characteristics of collision-zone magmatism. In: Coward, M.P., Ries, A.C. (Eds.), Collision Tectonics, 19. Geological Society London Special, Publication, pp. 67–81.
Hoskin, P.W.O., Schaltegger, U., 2003. The composition of zircon and igneous and metamorphic petrogenesis. In: Manchar, J.M., Hoskin, P.W.O. (Eds.), Zircon: Reviews of Mineralogy and Geochemistry, 53, pp. 27–62.
Hou, Z.-Q., Gao, Y.-F., Qu, X.-M., Rui, Z.-Y., Mo, X.-X., 2004. Origin of adakitic intrusives generated during mid-Miocene east–west extension in southern Tibet. Earth and Planetary Science Letters 220, 139–155.
Hou, M.L., Jiang, Y.H., Jiang, S.Y., Ling, H.F., Zhao, K.D., 2007. Contrasting origin of Late Mesozoic adakitic granitoids from the northwestern Jiaodong Peninsula, east China: implications for crustal thickening to delamination. Geological Magazine 144, 619–631.
Ishizuka, O., Taylor, R.N., Yuasa, M., Milton, J.A., Nesbitt, R.W., Uto, K., Sakamoto, I., 2007. Processes controlling along-arc isotopic variation of the southern Izu–Bonin arc. Geochemistry, Geophysics, Geosystems, 8 (http://dx.doi.org/10.1029/2006GC001475).
Kamei, A., Miyake, Y., Owada, M., Kimura, J.-I., 2009. A pseudo adakite derived from partial melting of tonalitic to granodioritic crust, Kyushu, southwest Japan arc. Lithos 112, 615–625.
Kay, R.W., 1978. Aleutian magnesian andesites: melts from subducted Pacific Ocean crust. Journal of Volcanology and Geothermal Research 4, 117–132.
Kay, S.M., Mpodozis, C., Ramos, V.A., Munizaga, F., 1991. Magma source variations for mid-late Tertiary magmatic rocks associated with a shallowing subduction zone and a thickening crust in the central Andes (28 to 33°S). Geological Society of America, Special Paper 265, 113–137.
Kay, S.M., Ramos, V.A., Marquez, M., 1993. Evidence in Cerro Pampa volcanic rocks of slab melting prior to ridge trench collision in southern South America. Journal of Geology 101, 703–714.
Khalatbari Jafari, M., Babaie, H.A., Gani, M., 2013. Geochemical evidence for Late Cretaceous marginal arc-to-backarc transition in the Sabzevar ophiolitic extrusive sequence, northeast Iran. Journal of Asian Earth Sciences 70–71, 209–230.
Khan, S.D., Walker, D.J., Hall, S.A., Burke, K.C., Shah, M.T., Stockli, L., 2009. Did the Kohistan–Ladakh island arc collide first with India? Geological Society of America Bulletin 121, 366–384.
Klemme, S., Prowatke, S., Hametner, K., Günther, D., 2005. Partitioning of trace elements between rutile and silicate melts: implications for subduction zones. Geochimica et Cosmochimica Acta 69, 2361–2371.
Kolb, M., Von Quadt, A., Peytcheva, I., Heinrich, C.A., Fowler, S.J., Cvetkovic, V., 2013. Adakite-like and normal arc magmas: distinct fractionation paths in the east Serbian segment of the Balkan–Carpathian Arc. Journal of Petrology 54, 421–451.
Li, W.-X., Li, X.-H., 2003. Adakitic granites within the NE Jiangxi ophiolites, south China: geochemical and Nd isotopic evidence. Precambrian Research 122, 29–44.
Li, J.-X., Qin, K.-Z., Li, G.-M., Xiao, B., Chen, L., Zhao, J.-X., 2011. Post-collisional ore-bearing adakitic porphyries from Gangdese porphyry copper belt, southern Tibet: melting of thickened juvenile arc lower crust. Lithos 126, 265–277.
Macpherson, C.G., Dreher, S.T., Thirlwall, M.F., 2006. Adakites without slab melting: high pressure processing of basaltic island arc magma, Mindanao, the Philippines. Earth and Planetary Science Letters 243, 581–593.
Martin, H., 1999. Adakitic magmas: modern analogues of Archaean granitoids. Lithos 46, 411–429.
Martin, H., Smithies, R.H., Rapp, R., Moyen, J.-F., Champion, D., 2005. An overview of adakite, tonalite–trondhjemite–granodiorite (TTG), and sanukitoid: relationships and some implications for crustal evolution. Lithos 79, 1–24.
Mazhari, S.A., Bea, F., Amini, S., Ghalamghash, J., Molina, J.F., Montero, P., Scarrow, J.H., Williams, I.S., 2009. The Eocene bimodal Piranshahr massif of the Sanandaj–Sirjan Zone, NW Iran: a marker of the end of the collision in the Zagros orogen. Journal of the Geological Society 166, 53–69.
McCall, G.J.H., 1997. The geotectonic history of the Makran and adjacent areas of southern Iran. Journal of Asian Earth Sciences 15, 517–531.
McCall, G.J.H., Kidd, R.G.W., 1982. The Makran, south-eastern Iran, the anatomy of a convergent plate margin, active from the Cretaceous to the Present. Geological Society, London, Special Publications 10, 387–397.
Middlemost, E.A.K., 1994. Naming materials in the magma/igneous rock system. Earth Science Reviews 37, 215–224.
Mohajjel, M., Fergusson, C.L., 2000. Dextral transpression in Late Cretaceous continental collision, Sanandaj–Sirjan zone, western Iran. Journal of Structural Geology 22, 1125–1139.
Mohajjel, M., Fergusson, C.L., Sahandi, M.R., 2003. Cretaceous–Tertiary convergence and continental collision, Sanandaj–Sirjan zone, western Iran. Journal of Asian Earth Sciences 21, 397–412.
Najman, Y., Pringle, M., Godin, L., Oliver, G., 2001. Dating of the oldest continental sediments from the Himalayan foreland basin. Nature 410, 194–197.
Nebel, O., Vroon, P.Z., van Westrenen, W., Iizuka, T., Davies, G.R., 2011. The effect of sediment recycling in subduction zones on the Hf isotope character of new arc crust, Banda arc, Indonesia. Earth and Planetary Science Letters 303, 240–250.
Omrani, H., Moazzen, M., Oberhänsli, R., Altenberger, U., Lange, M., 2013. The Sabzevar blueschists of the North-Central Iranian micro-continent as remnants of the Neotethys-related oceanic crust subduction. International Journal of Earth Sciences 102, 1491–1512.
Paces, J.B., Miller, J.D., 1993. Precise U–Pb age of Duluth Complex and related mafic intrusions, northeastern Minnesota: geochronological insights into physical, petrogenetic, paleomagnetic, and tectonomagmatic processes associated with the 1.1 Ga Midcontinent Rift System. Journal of Geophysical Research 98, 13997–14013.
Pang, K.-N., Chung, S.-L., Zarrinkoub, M.H., Mohammadi, S.S., Yang, H.-M., Chu, C.-H., Lee, H.-Y., Lo, C.-H., 2012. Age, geochemical characteristics and petrogenesis of Late Cenozoic intraplate alkali basalts in the Lut–Sistan region, eastern Iran. Chemical Geology 306–307, 40–53.
Pang, K.-N., Chung, S.-L., Zarrinkoub, M.H., Khatib, M.M., Mohammadi, S.S., Chiu, H.-Y., Chu, C.-H., Lee, H.-Y., Lo, C.-H., 2013. Eocene–Oligocene post-collisional magmatism in the Lut–Sistan region, eastern Iran: magma genesis and tectonic implications. Lithos 180–181 (234–251).
Peacock, S.M., Rushmer, T., Thompson, A.B., 1994. Partial melting of subducting oceanic crust. Earth and Planetary Science Letters 121, 227–244.
Petford, N., Atherton, M., 1996. Na-rich partial melts from newly underplated basaltic crust: the Cordillera Blanca Batholith, Peru. Journal of Petrology 37, 1491–1521.
Plank, T., Langmuir, C.H., 1998. The chemical composition of subducting sediment and its consequences for the crust and mantle. Chemical Geology 145, 325–394.
Prowatke, S., Klemme, S., 2006. Trace element partitioning between apatite and silicate melts. Geochimica et Cosmochimica Acta 70, 4513–4527.
Quidelleur, X., Grove, M., Lovera, O.M., Harrison, T.M., Yin, A., Ryerson, F.J., 1997. Thermal evolution and slip history of the Renbu Zedong thrust, southeastern Tibet. Journal of Geophysical Research 102, 2659–2679.
Rapp, R.P., Watson, E.B., Miller, C.F., 1991. Partial melting of amphibolite/eclogite and the origin of Archean trondhjemites and tonalites. Precambrian Research 51, 1–25.
Rapp, R.P., Watson, E.B., 1995. Dehydration melting of metabasalt at 8–32 kbar: implication for continental growth and crust–mantle recycling. Journal of Petrology 36, 891–931.
Rollinson, H.R., 1993. Using Geochemical Data: Evaluation, Presentation, Interpretation. Longman Scientific and Technical John Wiley Sons, New York (352 pp).
Rossetti, F., Nasrabady, M., Vignaroli, G., Theye, T., Gerdes, A., Razavi, M.H., Moin Vaziri, H., 2010. Early Cretaceous migmatitic mafic granulites from the Sabzevar range (NE Iran): implications for the closure of the Mesozoic peri-Tethyan oceans in central Iran. Terra Nova 22, 26–34.
Rossetti, F., Nasrabady, M., Theye, T., Gerdes, A., Monié, P., Lucci, F., Vignaroli, G., 2014. Adakite differentiation and emplacement in a subduction channel: the late Paleocene Sabzevar magmatism (NE Iran). Geological Society of America Bulletin. http://dx.doi.org/10.1130/B30913.1.
Rowley, D.B., 1996. Age of collision between India and Asia: a review of the stratigraphic data. Earth and Planetary Science Letters 145, 1–13.
Saccani, E., Delavari, M., Beccaluva, L., Amini, S., 2010. Petrological and geochemical constraints on the origin of the Nehbandan ophiolitic complex (eastern Iran): implication for the evolution of the Sistan Ocean. Lithos 117, 209–228.
Saccani, E., Allahyari, K., Beccaluva, L., Bianchini, G., 2013. Geochemistry and petrology of the Kermanshah ophiolites (Iran): implication for the interaction between passive rifting, oceanic accretion, and plume-components in the Southern Neo-Tethys Ocean. Gondwana Research 24, 392–411.
Sadeghian, M., Bouchez, J.L., Nédélec, A., Siqueira, R., Valizadeh, M.V., 2005. The granite pluton of Zahedan (SE Iran): a petrological and magnetic fabric study of a syntectonic sill emplaced in a transtensional setting. Journal of Asian Earth Sciences 25, 301–327.
Sajona, F.G., Maury, R.C., Bellon, H., Cotten, J., Defant, M.J., Pubellier, M., 1993. Initiation of subduction and the generation of slab melts in western and eastern Mindanao, Philippines. Geology 21, 1007–1010.

Schmitt, A.K., Grove, M., Harrison, T.M., Lovera, O.M., Hulen, J., Walters, M., 2003a. The Geysers–Cobb Mountain Magma System, California (Part 1): U–Pb zircon ages of volcanic rocks, conditions of zircon crystallization and magma residence times. Geochimica et Cosmochimica Acta 67, 3423–3442.

Schmitt, A.K., Grove, M., Harrison, T.M., Lovera, O.M., Hulen, J., Walters, M., 2003b. The Geysers–Cobb Mountain Magma System, California (Part 2): timescales of pluton emplacement and implications for its thermal history. Geochimica et Cosmochimica Acta 67, 3443–3458.

Sengör, A.M.C., Kidd, W.S.F., 1979. Post-collisional tectonics of the Turkish–Iranian plateau and a comparison with Tibet. Tectonophysics 55, 361–376.

Sengör, A.M.C., Altiner, D., Cin, A., Ustaomer, T., Hsu, K.L., 1988. Origin and assembly of the Tethyside orogenic collage at the expense of Gondwana Land. Geological Society of London, Special Publication 37, 119–181.

Şengör, A.M.C., 1990. A new model for the late Palaeozoic–Mesozoic tectonic evolution of Iran and implications for Oman. Geological Society, London, Special Publications 49, 797–831.

Shafaii Moghadam, H., Stern, R.J., 2011. Geodynamic evolution of upper Cretaceous Zagros ophiolites: formation of oceanic lithosphere above a nascent subduction zone. Geological Magazine 148, 762–801.

Shafaii Moghadam, H., Stern, R.J., Chiaradia, M., Rahgoshay, M., 2013. Geochemistry and tectonic evolution of the Late Cretaceous Gogher–Baft ophiolite, central Iran. Lithos 168–169, 33–47.

Shaw, D.M., 1970. Trace element fractionation during anatexis. Geochimica et Cosmochimica Acta 34, 237–243.

Smithies, R.H., 2000. The Archean tonalite–trondhjemite–granodiorite (TTG) series is not an analogue of Cenozoic adakite. Earth and Planetary Science Letters 182, 115–125.

Stampfli, G.M., 2000. Tethyan oceans. In: Bozkurt, E., Winchester, J.A., Piper, J.D.A. (Eds.), Tectonics and magmatism in Turkey and surrounding area. Geological Society Special Publication, 173, pp. 1–23.

Stern, C.R., Kilian, R., 1996. Role of the subducted slab, mantle wedge and continental crust in the generation of adakites from the Andean Austral Volcanic Zone. Contributions to Mineralogy and Petrology 123, 263–281.

Stöcklin, J., 1968. Structural history and tectonics of Iran: a review. American Association of Petroleum Geologist Bulletin 52, 1229–1258.

Stöcklin, J., 1977. Structural correlation of the alpine ranges between Iran and Central Asia. Société géologique de France, Paris, Mémoire hors série 8, 333–353.

Sun, S.S., McDonough, W.E., 1989. Chemical and isotopic systematics of oceanic basalts: implications for mantle composition and processes. In: Saunders, A.D., Norry, M.J. (Eds.), Magmatism in the Ocean Basins. Geological Society Special Publication, 42, pp. 313–345.

Tirrul, R., Bell, I.R., Griffis, R.J., Camp, V.E., 1983. The Sistan suture zone of eastern Iran. Geological Society of America Bulletin 94, 134–150.

Tirrul, R., Johns, J.W., Willoughby, N.O., Camp, V.E., Griffis, R.J., Bell, I.R., Meixner, H.M.,1989. Geological map of Nehbandan. Scale 1/100000. Geological survey of Iran.

Topuz, G., Altherr, R., Schwarz, W.H., Siebel, W., Satır, M., Dokuz, A., 2005. Post-collisional plutonism with adakite-like signatures: the Eocene Saraycık granodiorite (Eastern Pontides, Turkey). Contributions to Mineralogy and Petrology 150, 441–455.

Topuz, G., Okay, A.I., Altherr, R., Schwarz, W.H., Siebel, W., Zack, T., Satır, M., Şen, C., 2011. Post-collisional adakite-like magmatism in the Ağvanis Massif and implications for the evolution of the Eocene magmatism in the Eastern Pontides (NE Turkey). Lithos 125, 131–150.

Treloar, P.J., Izatt, C.N., 1993. Tectonics of the Himalayan collision between the Indian plate and the Afghan block: a synthesis. In: Treloar, P.J., Searle, M.P. (Eds.), Himalayan Tectonics: Geological Society of London Special. Publication, 74, pp. 69–87.

Tsuchiya, N., Kanisawa, S., 1994. Early Cretaceous Sr-rich silicic magmatism by slab melting in the Kitakami Mountains, Northeast Japan. Journal of Geophysical Research 99, 22205–22220.

Tsuchiya, N., Kimura, J.-I., Kagami, H., 2007. Petrogenesis of Early Cretaceous adakitic granites from Kitakami Mountains, Japan. Journal of Volcanology and Geothermal Research 167, 134–159.

Villemant, B., Jaffrezic, H., Joron, J.L., Treuil, M., 1981. Distribution coefficients of major and trace elements; fractional crystallization in the alkali basalt series of Chaine des Puys (Massif Central, France). Geochimica et Cosmochimica Acta 45, 1997–2016.

Walker, R.T., Gans, P., Allen, M.B., Jackson, J., Khatib, M., Marsh, N., Zarrinkoub, M., 2009. Late Cenozoic volcanism and rates of active faulting in eastern Iran. Geophysical Journal International 177, 783–805.

Wang, Q., McDermott, F., Xu, J.F., Bellon, H., Zhu, Y.T., 2005. Cenozoic K-rich adakitic volcanic rocks in the Hohxil area, northern Tibet: lower-crustal melting in an intracontinental setting. Geology 33, 465–468.

Wilmsen, M., Fürsich, F.T., Seyed-Emami, K., Majidifard, M.R., Taheri, J., 2009. The Cimmerian Orogeny in northern Iran: tectono-stratigraphic evidence from the foreland. Terra Nova 21, 211–218.

Zanchi, A., Zanchetta, S., Berra, F., Mattei, M., Garzanti, E., Molyneux, S., Nawab, A., Sabouri, J., 2009. The Eo-Cimmerian (Late? Triassic) orogeny in North Iran. Geological Society Special Publications 312, 31–55.

Zarrinkoub, M.H., Chung, S.-L., Chiu, H.-Y., Mohammadi, S.S., Khatib, M., Lin, I.-J., 2010. Zircon U–Pb Age and Geochemical Constraints from the Northern Sistan Suture Zone on the Neotethyan Magmatic and Tectonic Evolution in Eastern Iran. Abstract to GSA Conference on "Tectonic Crossroads: Evolving Orogens in Eurasia–Africa–Arabia", Oct. 4–8, 2010, p. 520 (Ankara, Turkey).

Zarrinkoub, M.H., Pang, K.-N., Chung, S.-L., Khatib, M., Mohammadi, S.S., Chiu, H.-Y., Lee, H.-Y., 2012. Zircon U–Pb age and geochemical constraints on the origin of the Birjand ophiolite, Sistan suture zone, eastern Iran. Lithos 154, 392–405.

Zeng, L., Gao, L.-E., Xie, K., Liu-Zeng, J., 2011. Mid-Eocene high Sr/Y granites in the Northern Himalayan Gneiss Domes: melting thickened lower continental crust. Earth and Planetary Science Letters 303, 251–266.

Zhu, B., Kidd, W.S.F., Rowley, D.B., Currie, B.S., Shafique, N., 2005. Age of initiation of the India–Asia collision in the east central Himalaya. The Journal of Geology 113, 265–285.

Zhu, D.-C., Zhao, Z.-D., Pan, G.-T., Lee, H.-Y., Kang, Z.-Q., Liao, Z.-L., Wang, L.-Q., Li, G.-M., Dong, G.-C., Liu, B., 2009. Early Cretaceous subduction-related adakite-like rocks of the Gangdese belt, southern Tibet: products of slab melting and subsequent melt-peridotite interaction? Journal of Asian Earth Sciences 34, 298–309.